Development of Mechanical Optical Clearing Devices for Improved Light Delivery in Optical Diagnostics

William Charles Vogt

Dissertation submitted to the faculty of the Virginia Polytechnic Institute and State University in fulfillment of the requirements for the degree of

Doctor of Philosophy
In
Biomedical Engineering

Christopher G. Rylander
Stephen M. LaConte
John L. Robertson
Ge Wang
Jessica Sparks

July 22nd, 2013
Blacksburg, VA

Keywords: optical clearing, biomechanics, indentation, finite element, Monte Carlo, numerical, near-infrared spectroscopy, diffuse reflectance spectroscopy, neuroimaging

Development of Mechanical Optical Clearing Devices for Improved Light Delivery in Optical Diagnostics

William Charles Vogt

Abstract

Biomedical optics is a rapidly expanding field of research focusing on the development of methods to detect, diagnose, and treat disease using light. While there are a myriad of optical systems that have been developed for biological tissue imaging, optical diagnostics, and optical therapeutics, all of these methods suffer severely limited penetration depths due to attenuation of light by tissue constituent chromophores, including cells, water, blood, and protein structures. Tissue optical clearing is a recent area of study within biomedical optics and photonics, where chemical agents have been used to alter tissue optical properties, reducing optical absorption and scattering and enabling light delivery to and collection from deeper tissue regions. However, there are concerns as to the safety and efficacy of these chemical clearing agents *in vivo*, especially in the skin, where the projective barrier function of the stratum corneum must be removed.

Mechanical optical clearing is a recently developed technology which utilizes mechanical loading to reversibly modify light transport through soft tissues, and much of the work published on this technique has focused on applications in skin tissue. This clearing technique enables deeper light delivery into soft tissues but does not require use of exogenous chemicals, nor does it compromise the skin barrier function. While this clearing effect is thought to be resultant from interstitial water and blood transport, the underlying mechanism has not been concretely identified nor characterized.

The hypothesis of this body of work was that interstitial transport of tissue chromophores (*e.g.* water and blood) causes intrinsic optical property changes, reduces tissue optical absorption and scattering, and improves light delivery in diagnostic applications. To test this hypothesis, we first developed a mathematical framework to simulate mechanical optical clearing, using both mechanical finite element models and optical Monte Carlo simulations. By directly simulating interstitial water transport in response to loading, data from mechanical simulations was

combined with optical Monte Carlo simulations, which enabled prediction of light transmission measurements made during mechanical indentation experiments. We also investigated changes in optical properties during mechanical indentation using diffuse reflectance spectroscopy. These studies used controlled flat indentation by a fiberoptic probe to dynamically measure intrinsic optical properties as they changed over time. Finally, we apply mechanical optical clearing principles to functional near-infrared spectroscopy for neuroimaging. By building a prototypical mechanical optical clearing device for measuring cerebral hemodynamics, we demonstrated that mechanical optical clearing devices modify measured cerebral hemodynamic signals in human subjects, improving signal quality.

Acknowledgments

While this dissertation contains the body of my research over the past four years, it is not a work which I could have completed on my own. I would like to thank my advising committee for their hard work and for supporting me through these endeavors. Dr. Sparks, thank you for providing your expertise in finite element modeling of soft tissues, especially your insight in correctly implementing these models in the Abaqus software package. Our conversations probably saved me months of digging through the Abaqus theory manual and the biomechanics literature. Dr. Wang, thank you for devoting your time and resources for my optical modeling efforts, and for your insights into the potential applications of our technology. Dr. LaConte, thank you for beginning an exciting collaborative project to develop a target application for our technology; I hope that this team will continue to advance mechanical optical clearing for neuroimaging. Dr. Robertson, thanks for keeping our eye on the prize, brainstorming potential applications, and for your help in developing our current histology arrangement. Finally, thank you Dr. Rylander for your dedication to my success. You taught me optics, you taught me project management, you taught me scientific vision. Your mentoring was critical to my development as a young researcher, and for that I'm truly grateful.

I would also like to thank the administrative team at SBES for their support. Thank you Tess, Kathy, Pam, Jo, and Monika for all of your help, no matter the deadline or the time of day you were always willing to lend a hand, and for that I'm deeply grateful. I'd especially like to thank Kathy for keeping the reimbursements flowing smoothly (despite my best efforts to ruin them). Tess, thank you so much for helping me through all that paperwork, making my degree completion at all possible.

Of course, thanks are also in order for my current and former labmates, Lyle Hood, Abhijit Gurjarpadhye, Rudy Andriani, Alondra Izquierdo-Román, Alp Kosoglu, Emily Brandon, Egleide Elenes, and Charles Smith. Thank you Alondra, Abhijit, and Rudy for your specific contributions to this body of work, and thanks to all of my labmates for creating a great team and work environment.

I've made so many friends during my time at Virginia Tech, inside and outside of lab (but for most, we saw each other under both conditions). I'd like to thank Lyle, Kate, Rudy, Matt, Patrick, Kristen, Paulo, Chuquin, Matthias, Bryce, Lucas, Brandon, Mike, Szot, Arena,

Brad, Rory, and Laura for all the fun times, not to mention our time talking shop, coming up with crazy ideas, and a few discussions that helped me through some tricky challenges in my studies.

Finally, I'd like to acknowledge the loving support of my parents and my girlfriend, Emma. Mom and Dad, thanks for all the phone calls, for keeping interested in my research, for listening to me rant about the hard times, and for keeping tabs on me as I cavorted across the country attending who knows what conference. I love you both so much. Emma, you are my rock. A chance to see you was the single thing I most looked forward to every day. You've always been there for the adventures, and you've always been there to provide a smile (and sometimes food) when I needed it most. I love you with all I've got, and I can't wait to start our life together.

Table of Contents

List of Figures

List of Tables

Chapter 1. Overview

1.1 Biomedical Optics and Tissue Diagnostics

Biomedical optics is a growing area of research focusing on the application of optical systems and techniques for characterizing biological tissues and detecting diseases. Diffuse optical spectroscopic techniques have become prevalent in the literature due to their ability to acquire reflectance spectra that provide information about tissue biochemistry and physiology. Light-based diagnostic techniques possess many advantages over other imaging modalities; optical imaging and spectroscopic techniques use safe, non-ionizing radiation to measure light transport through a biological medium, can differentiate between soft tissues of various types and disease states through changes in absorption and scattering behavior, and are relatively low-cost imaging systems.

Despite these advantages, all optical diagnostic techniques are limited in efficacy due to the attenuation of light in biological tissues due to diffuse scattering and absorption by various constituent chromophores such as water, blood and proteins. "Tissue optical clearing" is a new field of research that focuses on methods for reducing light scattering in turbid biological tissues in order to enable deep light delivery for therapeutic or diagnostic applications. While most optical clearing research has focused on the use of exogenous chemical agents, mechanical optical clearing is a promising technology that utilizes mechanical loading to noninvasively and reversibly modify tissue optical properties.

1.2 Project Objectives

Mechanical loading has been shown to affect light transport in turbid biological tissues. However, the fundamental mechanisms behind this effect must be elucidated in order to guide device development and translation to biomedical applications. The overarching hypothesis of this research proposal is that interstitial transport of tissue chromophores (*e.g.* water and blood) causes intrinsic optical property changes, reduces tissue optical absorption and scattering, and improves light delivery in diagnostic applications. This hypothesis will be evaluated by:

1) Developing a multidomain mathematical model of mechanical optical clearing, including poroviscoelastic mechanical finite element models and optical Monte Carlo simulation,

2) Measuring tissue optical properties during mechanical deformation using diffuse reflectance spectroscopy, and

3) Applying mechanical optical clearing to functional near-infrared spectroscopy of cerebral hemodynamics.

1.3 Document Organization

This dissertation describes research focusing on development of mechanical optical clearing for biomedical applications. Chapter 2 provides an introduction to biomedical optics and tissue optics, describes current limitations of light delivery in biological tissues, and provides a literature review of chemical and mechanical optical clearing techniques. Chapter 3 describes the development of a combined mechanical/optical mathematical framework for investigating the fundamental mechanisms of action of mechanical optical clearing, as well as experimental mechanical and optical characterization of *ex vivo* porcine skin. Chapter 4 describes the use of diffuse reflectance spectroscopy, a broadly applicable optical diagnostic tool, for measuring tissue optical property changes during mechanical indentation. Chapter 5 describes the application of mechanical optical clearing to near-infrared spectroscopy for functional measurement of cerebral hemodynamics in human subjects. Chapter 6 discusses the results of this dissertation research and offers summary conclusions.

Chapter 2. Introduction

2.1 Introduction to Biomedical Optics

Medical imaging first began with the discovery of the X-ray by Wilhelm Roentgen in 1895, when Roentgen observed that X-rays traveled through human tissues of the hand with varying attenuation depending on tissue type [1]. Roentgen's early work identified barium as a suitable contrast agent for imaging, leading to X-ray fluoroscopy for medical imaging. Fluoroscopy enables X-ray imaging in real time, capturing patient motion, cannot acquire 3D images. This was accomplished by X-ray computed tomography (CT), which uses an X-ray source-detector array swept through a circular path to acquire tomographic image slices of a patient.

Nuclear magnetic resonance (NMR) was a phenomenon discovered in 1938 by Rabi *et al.* that was developed for analytical chemistry applications. With the discovery that NMR could distinguish between healthy and cancerous human tissues by Damadian in 1971 [2], NMR became the foundation for magnetic resonsnace imaging (MRI), an imaging system based on this effect. MRI enables functional imaging of tissues (*i.e.* imaging of blood transport, metabolism, other tissue functions) with high spatial resolution through the entire thickness of the human body.

However, there are some disadvantages to X-ray and magnetic resonance-based imaging modalities. These methods rely on the use of ionizing radiation, which is a known carcinogen and at high doses can also radiation burns and fatality via acute radiation syndrome [3]. These risks result in the necessity for strict regulation and control of radiation dose in both patients and physicians. These techniques also require expensive hardware, with CT scanners costing $200,000 to $700,000 and MRI suites costing $1,000,000 to $4,000,000.

Biomedical optics is a rapidly growing field of research focused on the development of light-based technologies for both diagnosing and treating disease. Light-based diagnostic techniques possess many advantages over other imaging modalities as shown in Table 1 . Optical imaging and spectroscopic techniques use safe, non-ionizing optical radiation to evaluate light transport through tissues. These methods can differentiate between soft tissues of various types and disease states through changes in optical absorption and scattering behavior [4]. Optical absorption measurements are particularly sensitive to changes in oxy- and deoxy-hemoglobin

concentrations as well as blood oxygen saturation, which can be useful in studying tissue growth, metabolism, and function. In particular, monitoring changes in hemodynamics and oxygenation can enable detection of angiogenesis and hypermetabolism, which are hallmarks of cancerous tissues [5]. Optical scattering measurements typically provide information on molecular size distributions [6] or tissue fiber orientation [7]. Optical imaging systems are also typically cheaper than CT or MRI systems by an order of magnitude due to their mass-produced electro-optic and opto-mechanical system components (*e.g.* diode lasers, light-emitting diodes (LEDs), fiberoptic cabling, lenses, etc).

Table 1. Comparison of various medical imaging modalities. Adapted from [4].

Characteristics	X-ray Imaging	Ultrasonography	MRI	Optical Imaging
Soft-tissue contrast	Poor	Good	Excellent	Excellent
Spatial resolution	Excellent	Good	Good	Mixed*
Maximum imaging depth	Excellent	Good	Excellent	Good
Function	None	Good	Excellent	Excellent
nonionizing radiation	No	No	Yes	Yes
Data acquisition	Fast	Fast	Slow	Fast
Cost	Low	Low	High	Low

***High in ballistic imaging and photoacoustic tomography, low in diffuse optical tomography.**

2.2 Fundamentals of Light-Tissue Interactions

While biomedical optics has grown significantly, the major challenge in optical imaging and diagnostics was and still is understanding the complex interactions between optical photons and tissue constituents, then using these concepts to improve light transport and increase the quality of recoverable information about the tissue of interest. In this section,

2.2.1 Light Sources

Delivery of optical energy into a biological tissue is governed by many factors, and the characteristics of the light source will influence subsequent light transport through turbid media. One major consideration is the degree of coherence of the light emitted by a source. Coherence is a property of electromagnetic waves defined as having interference that does not change in space or time. Coherence may be considered in either the spatial domain, where low coherence indicates spatial variations in wave interference, or the temporal domain, where low coherence indicates high variations of wave amplitude over time. Many optical systems use monochromatic continuous-wave (constant amplitude and wavelength) lasers because of their high spatial and temporal coherence as well as their efficient coupling with collimating lenses, resulting in a

Gaussian beam of photons traveling along the axis of the beam. The small spectral bandwidth (< 1 nm) of lasers also allows highly specific targeting of absorbing or fluorescent chromophores in biological media.

In other applications, diffuse sources, such as light-emitting diodes (LEDs), are used to deliver light over a large volume within tissues. LED chips may be ideally considered as Lambertian point sources that emit equally over all angles within a hemisphere, but these sources are incoherent, and emit light in a rapidly-diverging cone. LEDs also have much higher spectral bandwidth (~5-50 nm at full-width half-maximum) compared to lasers, which can reduce the efficacy of absorption-dependent imaging and spectroscopic techniques.

2.2.2 Tissue Optical Properties and Light-Tissue Interactions

Light transport through a turbid medium is determined by the intrinsic optical properties of that medium. The first property to consider is the refractive index, the ratio of the speed of light in vacuum to the speed of light of the medium. As light travels through an interface between media of different refractive indices, refraction will occur according to Snell's Law. For collimated light orthogonal to the tissue surface, there is negligible refraction, while a diffuse source would experience higher refraction. Although tissues are heterogeneous materials, they may be considered to have a group or bulk refractive index with a typical range of 1.3-1.5 depending on the relative volume fractions of tissue constituents and the optical properties of each constituent.

In turbid (light scattering) media, the particle model of light (where light consists of particles called photons) is useful for describing light-tissue interactions. As a photon travels through a medium, there is an increasing probability of interacting with a molecule within the medium. If this interaction occurs, there is a probability that the photon will be absorbed by the molecule and converted into some other form of energy (*e.g.* thermal energy, fluorescent remission at a different wavelength/energy content). The property describing this phenomenon is the optical absorption coefficient μ_a [mm^{-1}], which describes the average number of absorption events that occur per unit length inside the medium. If the medium is purely absorptive and non-scattering, the inverse of μ_a is equivalent to the mean free path (MFP), the average travel distance of a photon before absorption.

Another critical phenomenon in photon transport is scattering. As photons travel through an optical medium, they may interact with molecules and undergo elastic scattering, changing direction after interacting with a particle in the medium. The optical scattering coefficient, μ_s [mm^{-1}], represents the average number of scattering events per unit length. In elastic scattering, a photon becomes absorbed by a particle but then remitted without losing energy. However, because there is information loss during the absorption event, the photon is generally remitted on a different trajectory. The probability distribution function of the remitted trajectory can be described using a scattering phase function. For biological tissues, the Henyey-Greenstein function has been shown to best describe experimental data. This function calculates the probability distribution function of the remission trajectory, $p(\theta)$, as

$$p(\theta) = \frac{1}{4\pi}\frac{1-g^2}{[1+g^2-2g\cos(\theta)]^{3/2}}, \qquad \text{s.t.} \int_0^{2\pi}\int_0^{\pi} p(\theta)\sin(\theta)\,d\theta d\phi = 1 \qquad \text{Eq. (1)}$$

where θ [rad] is the angle relative to the initial trajectory and g [-] is the anisotropy factor, an intrinsic optical property that describes the scattering distribution. Positive values of g denote forward scattering media, while negative values of g denote backward scattering media. For $g = 0$, scattering is isotropic, with equal probability of remission in any direction from a scattering event, while $g = 1$ would represent remission only along the initial trajectory. Most tissues have anisotropy values from 0.7-0.9, indicating that these media are highly forward scattering. Figure 1 shows the Henyey-Greenstein phase function value with scattering angle for various values of g. It is often convenient to define a lumped parameter called the reduced scattering coefficient:

$$\mu_s' = \mu_s(1-g) \qquad \text{Eq. (2)}$$

In the visible and NIR wavelength ranges, the tissue scattering coefficient is typically much higher than the absorption coefficient, indicating scattering-dominated light transport, also known as the diffuse transport regime. However, for some wavelengths absorption is more significant due to an absorption peak of water or various hemoglobin species. As such, it is often important to consider a reduced total attenuation coefficient, $\mu_{t,}$ which combines attenuation from absorption and scattering events into a single parameter:

$$\mu_t = \mu_a + \mu_s' \qquad \text{Eq. (3)}$$

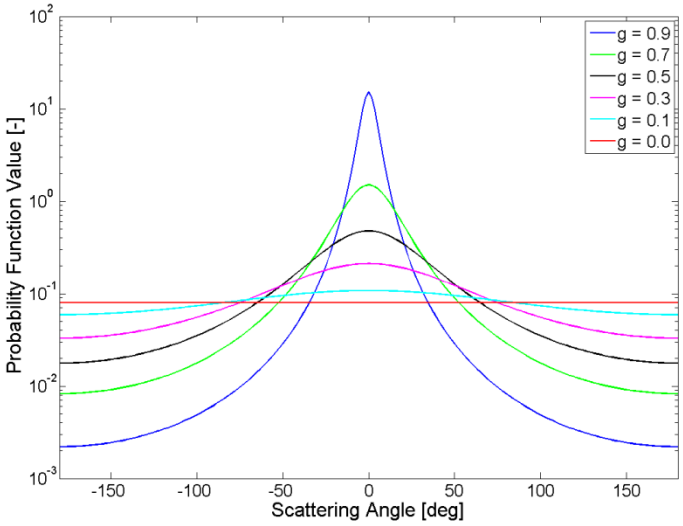

Figure 1. Scattering angle distribution defined by Henyey-Greenstein function for various values of *g*.

2.3 Limitations of Light Delivery in Biological Tissues

Optical diagnostic and therapeutic technologies are fundamentally limited due to heavy absorption and attenuation of light in biological tissues, resulting in low penetration depth and poor signal quality degradation in deeper tissue regions. Transmission of collimated light through tissues may be approximated using Beer's Law, an idealized description of one-dimensional light transmission through an absorbing media. Beer's Law states that the optical intensity as a function of depth in an optical medium, I(z), may be calculated as

$$I(z) = I_0 e^{-\mu_a z} \qquad \text{Eq. (4)}$$

Where I_0 is the incident irradiance on the tissue surface and z is the depth into the medium. The assumptions of this law are that 1) the medium is non-scattering and homogeneous, 2) incident light consists of parallel rays (highly collimated), 3) absorption events are independent, and 4) there are no emission effects resulting from excitation by input light. Biological media create deviations from Beer's Law because of their high scattering, heterogeneity, and emission due to fluorescence of extracellular proteins such as collagen.

The penetration depth, δ_t, of a collimated beam may be defined as the mean free path of an attenuation (both absorption and scattering) event as the depth at which the intensity is 36.7% (1/e) of the incident irradiance. In terms of the reduced total attenuation coefficient, μ_t, this may be written as

$$\delta_t = \frac{1}{\mu_t} = \frac{1}{(\mu_a + \mu_s')} \quad \text{Eq. (5)}$$

Because tissues are diffuse media, the effective penetration depth, δ_{eff}, is a better estimate of penetration depth. δ_{eff} is defined from the effective attenuation coefficient, μ_{eff}, as

$$\delta_{eff} = \frac{1}{\mu_{eff}} = \frac{1}{\sqrt{3\mu_a(\mu_a + \mu_s')}} \quad \text{Eq. (6)}$$

Figure 2 shows the optical properties and penetration depths as a function of wavelength for *ex vivo* porcine skin. Data were calculated from spectrophotometric data using inverse-adding doubling (see Chapter 3). From Figure 2(f), it is clear that optical penetration depth is greatest from ~600–1300 nm, often referred to as the 'optical window' for biomedical optics and agrees with published data [8, 9]. While biological tissues do not meet all the assumptions of Beer's law, tissues have been empirically observed to exhibit exponential attenuation in depth that may be described using $\mu_t$or μ_{eff} in place of μ_a depending on whether or not the tissue may be considered scattering-dominated (diffusion approximation) at the wavelength of interest.

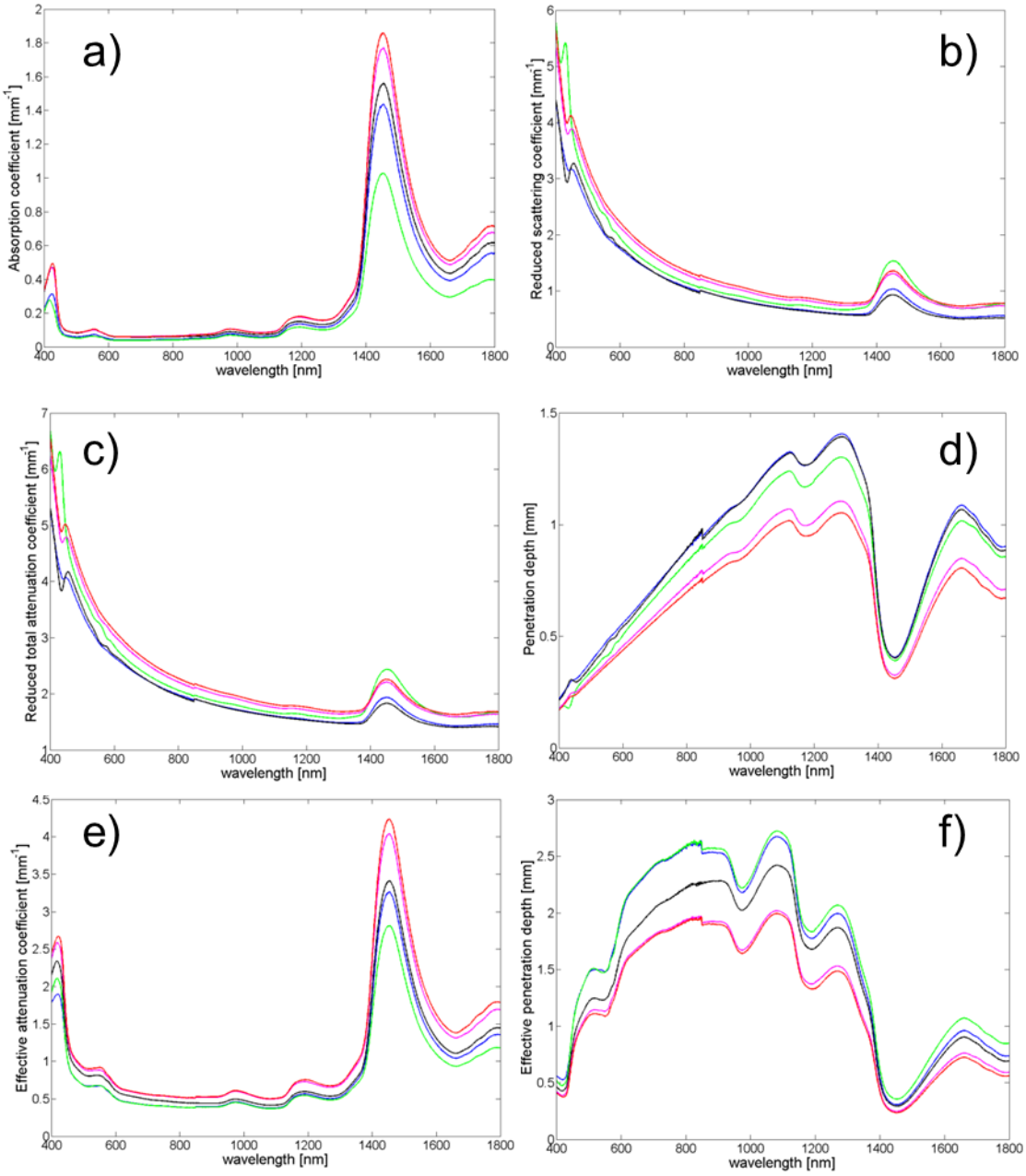

Figure 2. Optical properties of ex vivo porcine skin determined from spectrophotometry (N=5). a) Absorption coefficient, b) Reduced scattering coefficient, c) Reduced total attenuation coefficient, d) penetration depth, e) Effect attenuation coefficient, f) Effective penetration depth.

2.4 Chemical Optical Clearing

Biological tissues are heterogeneous materials primarily comprised of cells, water, blood, and proteins. This heterogeneity leads to high turbidity due to refractive index mismatches between various tissue constituents, including proteins, cells, water, and blood [10-13]. This

turbidity attenuates delivered light and prevents delivery of collimated light to deep tissue regions (*e.g.* tumors, blood vessels, subcutaneous fat beneath skin). Tissue scattering also reduces imaging resolution and signal quality as imaging depth increases. While tissue optical properties were traditionally considered constant, studies have shown that application of certain chemical agents can cause reversible reductions in tissue light scattering [10, 12, 14-16]. In the past 15 years, "chemical optical clearing agents" have been applied in many biological tissues, including ocular sclera [17], gastrointestinal tract [18, 19], muscle [20] and skin [9, 12, 16, 18, 21-24]. Chemical optical clearing can reduce tissue scattering and enable deeper light delivery for diagnostic or therapeutic applications. Chemical optical clearing has been shown to improve imaging for optical coherence tomography (OCT) [25, 26], two-photon microscopy [27], second harmonic generation imaging [28], and near-infrared reflectance spectroscopy [19].

While chemical optical clearing techniques are becoming frequently studied, there are still questions as to the mechanisms of chemical optical clearing. Early studies suggested that agents such as glycerol and polyethylene glycol replace interstitial pore water, reducing refractive index mismatch between pore fluid and the collagen matrix. The refractive index of tissue can range from 1.3-1.5 [29, 30]. Measurement of dry collagen refractive index determined that collagen is a birefringent material, with a refractive index of 1.38 in the axial direction and 1.51 in the radial direction [31]. Because water has a refractive index of 1.33, replacement by optical clearing agents substantially reduces refractive index mismatch between pore fluid and collagen by ~50%. Using the Lorentz-Lorenz rule of mixtures [32], it is possible to relate the refractive indices of tissue constituents (n_{water} and $n_{protein}$) to the bulk (average) refractive index, n_{skin} , based on the volume fraction (ϕ_{water} and $\phi_{protein}$) of each constituent:

$$\frac{{n_{skin}}^2 - 1}{{n_{skin}}^2 + 2} = \frac{{n_{water}}^2 - 1}{{n_{water}}^2 + 2}\phi_{water} + \frac{{n_{protein}}^2 - 1}{{n_{protein}}^2 + 2}(1 - \phi_{water}), \qquad \phi_{water} + \phi_{protein} = 1 \qquad \text{Eq. (7)}$$

Dehydration has also been proposed as a mechanism of optical clearing. Rylander *et al.* performed glycerol immersion and air immersion of rat skin and tail tendons. While glycerol immersion is a chemical clearing technique, air immersion does not replace interstitial pore water with another liquid; water is pulled out of the tissue due to osmotic pressure at the tissue surface, causing the tissue's porous structure to shrink, reducing pore volume and increasing matrix stiffness. Because air immersion, which operates only by dehydration, produced similar optical clearing effects to those of glycerol immersion, the authors concluded that dehydration is a necessary mechanism underlying chemical optical clearing.

Collagen dissociation is another potential mechanism for chemical optical clearing, first proposed by Yeh *et al.* [28, 33]. These studies determined through second harmonic generation imaging that collagen structures can be reversibly dissociated by exogenous chemicals including glycerol, which reduces scattering caused by the birefringent collagen fibrils. Hirshburg *et al.* [34] demonstrated a correlation between collagen solubility and optical clearing in rodent skin, indicating that good collagen solvents are better optical clearing agents. Recently, Hirshburg *et al.* [35] determined through Raman spectroscopy that chemical optical clearing is governed by disruption of the collagen hydration shell layer, and that replacing the hydration shell with optical clearing agents homogenizes the refractive index of the tissue.

While the mechanisms of chemical optical clearing have been extensively studied, there are still open questions about their clinical application. Chemical optical clearing requires delivery of exogenous chemicals to the body; with regards to skin tissue, the barrier function afforded by the stratum corneum to keep infectious microbes out of the tissue must be compromised. There have been several studies that have investigated improving chemical optical clearing techniques using other additional techniques, including sandpaper grinding [36], fractional ablation [37], light irradiation [38, 39], and chemical penetration enhancers [19, 40-42]. In addition, Yoon *et al*. reported the use of a microneedle roller to improve optical clearing agent permeation through microchannels created in *ex vivo* skin samples [43]. Xu *et al.* demonstrated that sonophoresis (ultrasound-enhanced drug delivery) could be used to enhance optical clearing in skin as evaluated using OCT [44]. Kang *et al.* performed a comparative study by investigating different combinations of large-area uniaxial compression, glycerol immersion, and microneedling [13]. They determined that combination of chemical immersion and compression yielded the largest increases in light transmission and beam profile quality.

2.5 Mechanical Optical Clearing

Mechanical optical clearing is a new technology that utilizes mechanical loading to reversibly modify tissue optical properties. Based on their earlier work investigating the dehydration mechanism of chemical optical clearing [6], Rylander *et al.* hypothesized that interstitial water transport due to applied mechanical force would cause optical clearing in compressed regions of tissue [45]. To test this hypothesis, they developed prototypical mechanical Tissue Optical Clearing Devices (TOCDs). TOCDs consisted of arrays of

hemispherical translucent indenters within a vacuum chamber. As suction is applied, tissue is pulled around the indenters, causing a reaction force to compress the tissue beneath the indenters, creating regions of modified optical properties (see figref). After applying TOCDs to *in vivo* human skin on the volar forearm, the device was removed and the skin was observed to redden in between indented regions, which may be indicative of blood accumulation (see Figure 3a-b). Indented regions were darker, suggesting that there was deeper light penetration with fewer remitted photons. Upon applying the TOCD to *ex vivo* porcine skin, the effect was repeated. Transmission-mode imaging of the optically cleared porcine skin showed increased delivery of white light through cleared regions compared with surrounding native tissue regions (see Figure 3c-d). TOCDs were also demonstrated to affect photothermal heat generation in the cleared regions, and this was thought to be due to changes in thermal properties caused by changes in relative constituent volume fractions, *e.g.* decreases in tissue water and blood content.

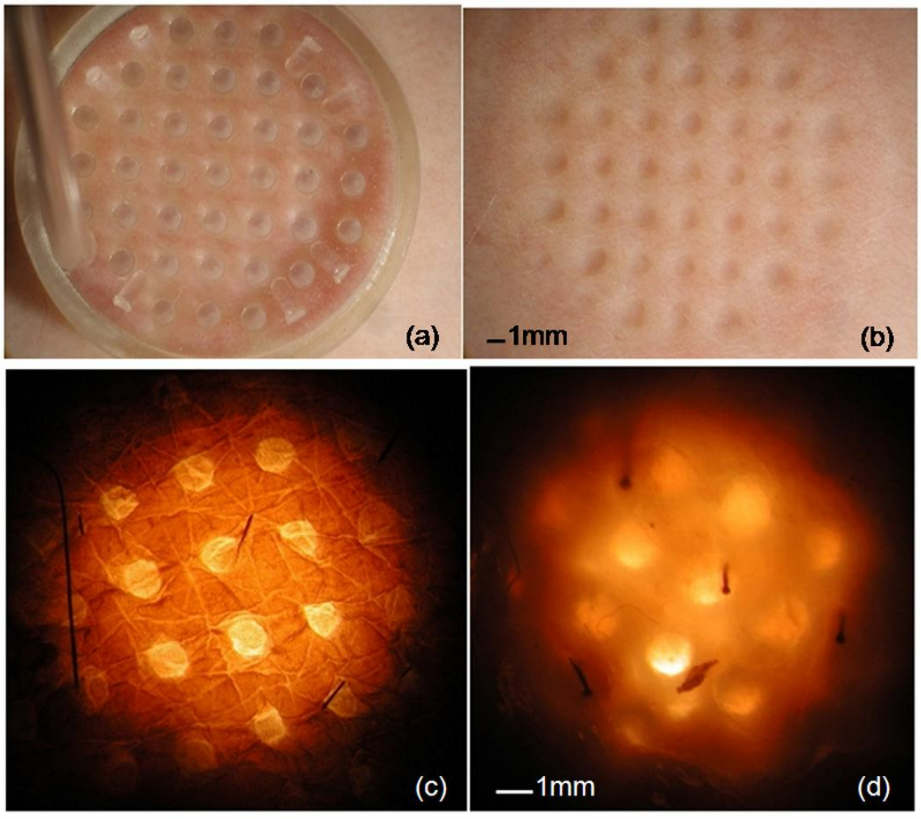

Figure 3. Photographs of in vivo human skin during application (a) and after removal (b) of the first TOCD prototype. Epidermal (c) and dermal (d) images of ex vivo porcine skin specimen trans-illuminated with visible light subsequent to application of the prototype to the epidermal surface [45]. Reprinted with permission from John Wiley & Sons Inc.

In another study by our group, Drew *et al.* evaluated optical clearing effects produced by TOCDs using Optical Coherence Tomography (OCT), a low-coherence interferometric imaging

technique capable of imaging turbid tissues at ~10 um resolution [46]. OCT signals can also be used to measure tissue thickness and depth-averaged refractive index using the technique of Sorin and Gray [47]. By employing the Lorentz-Lorenz rule of mixtures [32], the measured refractive index was related to tissue water volume fraction, with results indicating reduction of water content from ~70% to as low as 30% within tissue regions beneath the indenters (see Figure 4). As shown in Figure 5, OCT images captured in B-scanning mode (2D spatial imaging) and M-scanning mode (1D axial image over time, shown as a 2D image) demonstrated that TOCDs increase penetration depth of light, increasing signal strength and image quality in tissue regions beneath TOCD indenters. Another recent study from our group [48] refined this technique and investigated manual indentation of *in vivo* human skin. Results again showed increases in refractive index and reduction of calculated water volume fraction. OCT images also indicated thickness reduction of the stratum corneum and increased signal intensity measured at 1 mm optical depth (see Figure 6).

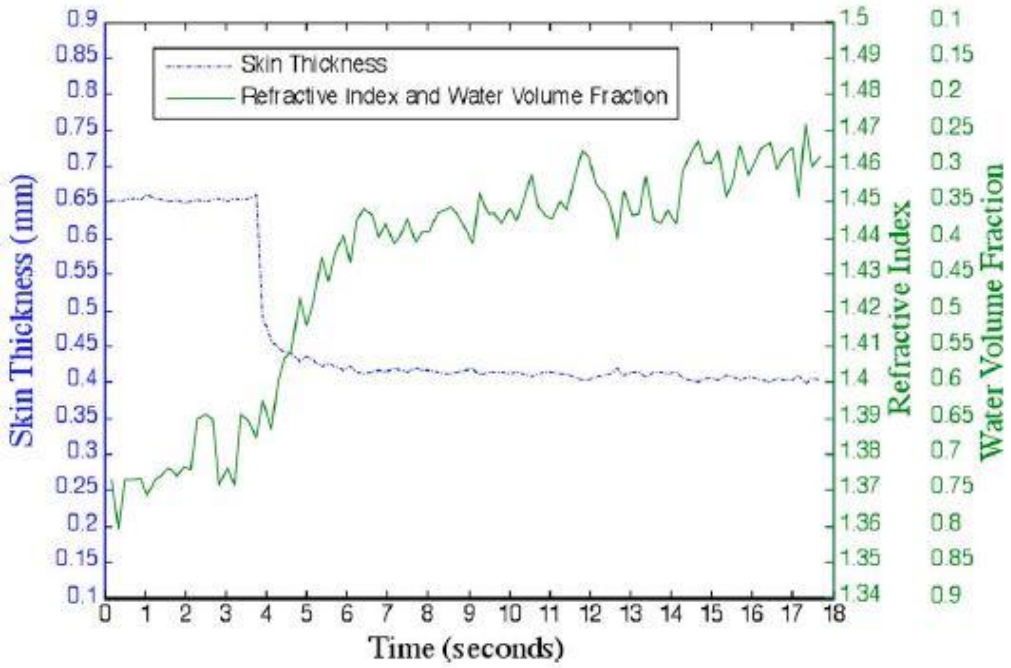

Figure 4. Skin thickness, mean group index, and water volume fraction versus time. Vacuum was applied to porcine skin after 4 s and continued through the 18-s time duration .

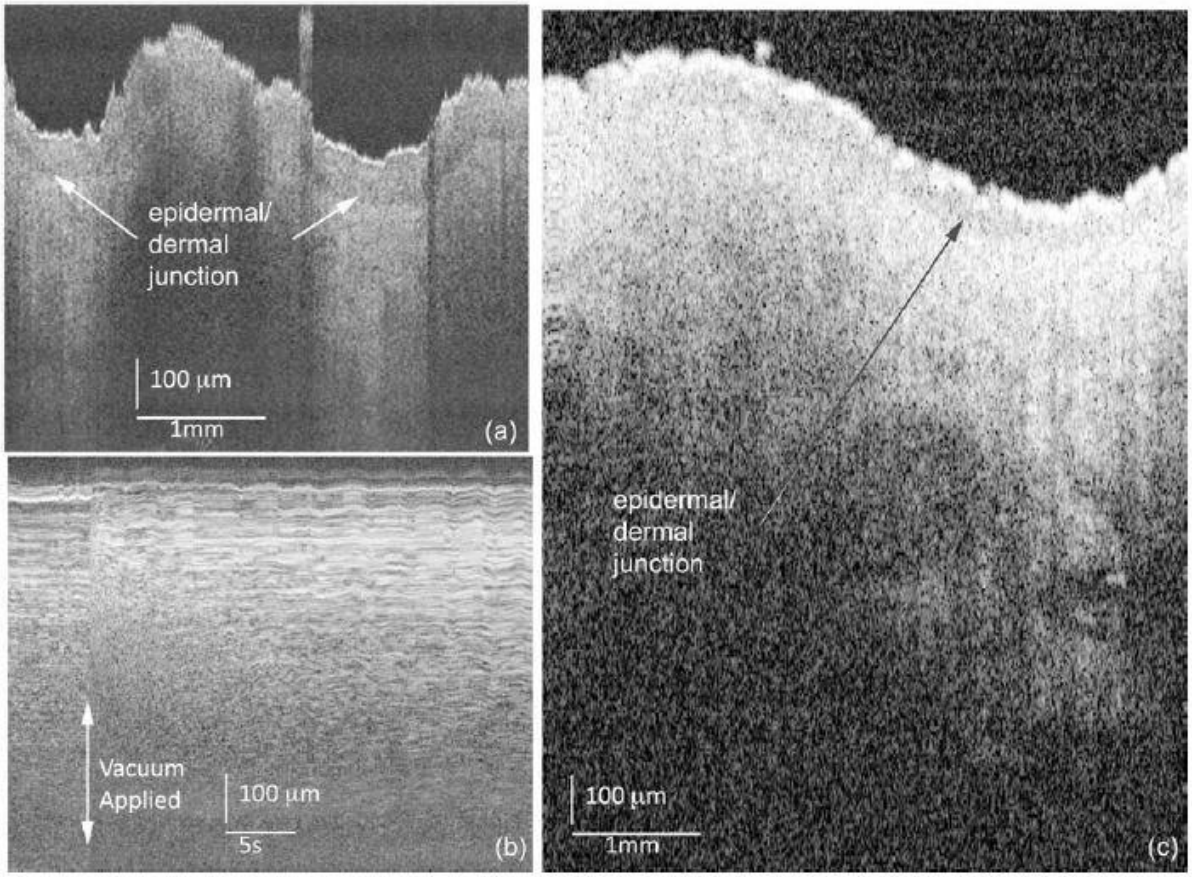

Figure 5. In vivo human skin: a) OCT B-scan image (850 nm) following application of the first TOCD. b) OCT M-scan image (1310 nm) before and during application of the first TOCD. c) OCT B-scan image (1310 nm) following application and removal of the second TOCD [46] Reprinted with permission from the Society of Photo Optical Instrumentation Engineers.

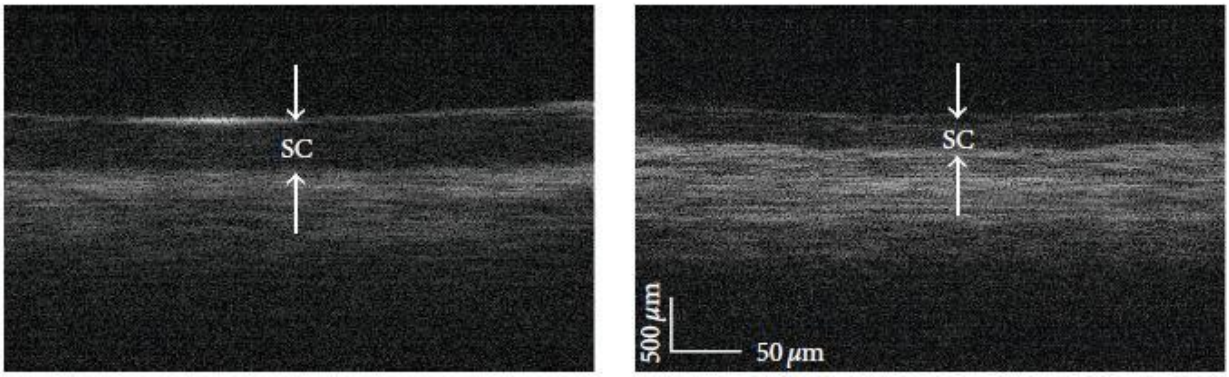

Figure 6. Representative OCT images and analysis of a human fingertip (a) before and (b) after compression. White arrows denote the stratum corneum (SC).

Mechanical optical clearing has also been evaluated using bright field microscopy [49]. In this study, we used manual indentation with a 5 mm hemispherical indenter to mechanically clear *ex vivo* porcine skin samples, which were then placed over a 1951 USAF resolution target containing spaced black and white lines at various line spacing frequencies. Resolution capability and Michelson contrast were calculated using two region of interest (ROI) techniques (see Figure 7). The study was also performed for skin samples chemically cleared using glycerol or dimethyl sulfoxide. As shown in Figures Figure 8 and Figure 9, results demonstrated that mechanical indentation allowed visualization of the target bars beneath the turbid skin samples, and mechanical optical clearing providing superior resolution and contrast than chemical optical clearing for the same target elements. Data showed that the maximum resolution and contrast increased with increased tissue strain. Mechanical optical clearing achieved higher maximum resolution and Michelson contrast sensitivity compared with chemical immersion techniques, which created morphology changes that hindered resolution of target bars.

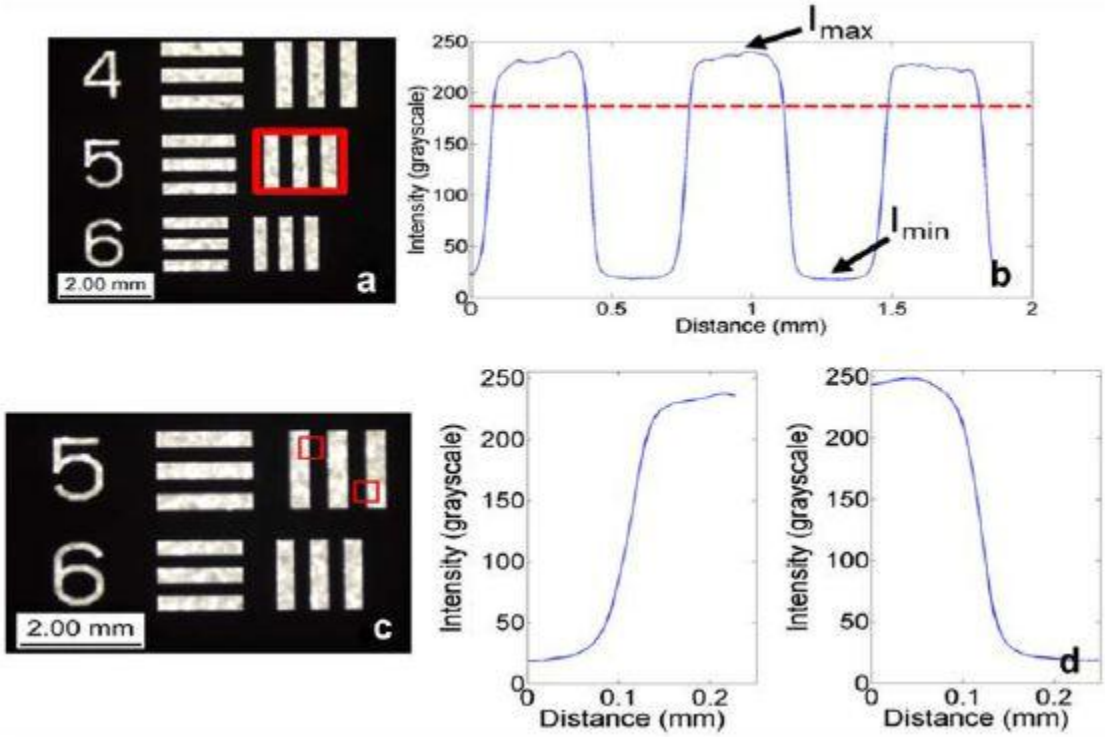

Figure 7. a) Image of USAF 1951 Target, Group 0, Elements 4–6. The ROI selected in the image (red box, method 1) was used to generate the intensity profile plot. b) Intensity profile plot. Peaks correspond to the white bars of the target ROI in a). Valleys represent the dark spaces between the target bars. The red line denotes Rayleigh's criterion for determining resolution. c) ROI selection method 2. d) Intensity profile plots corresponding to the ROI's shown in c) [49]. Reprinted with permission from John Wiley & Sons Inc.

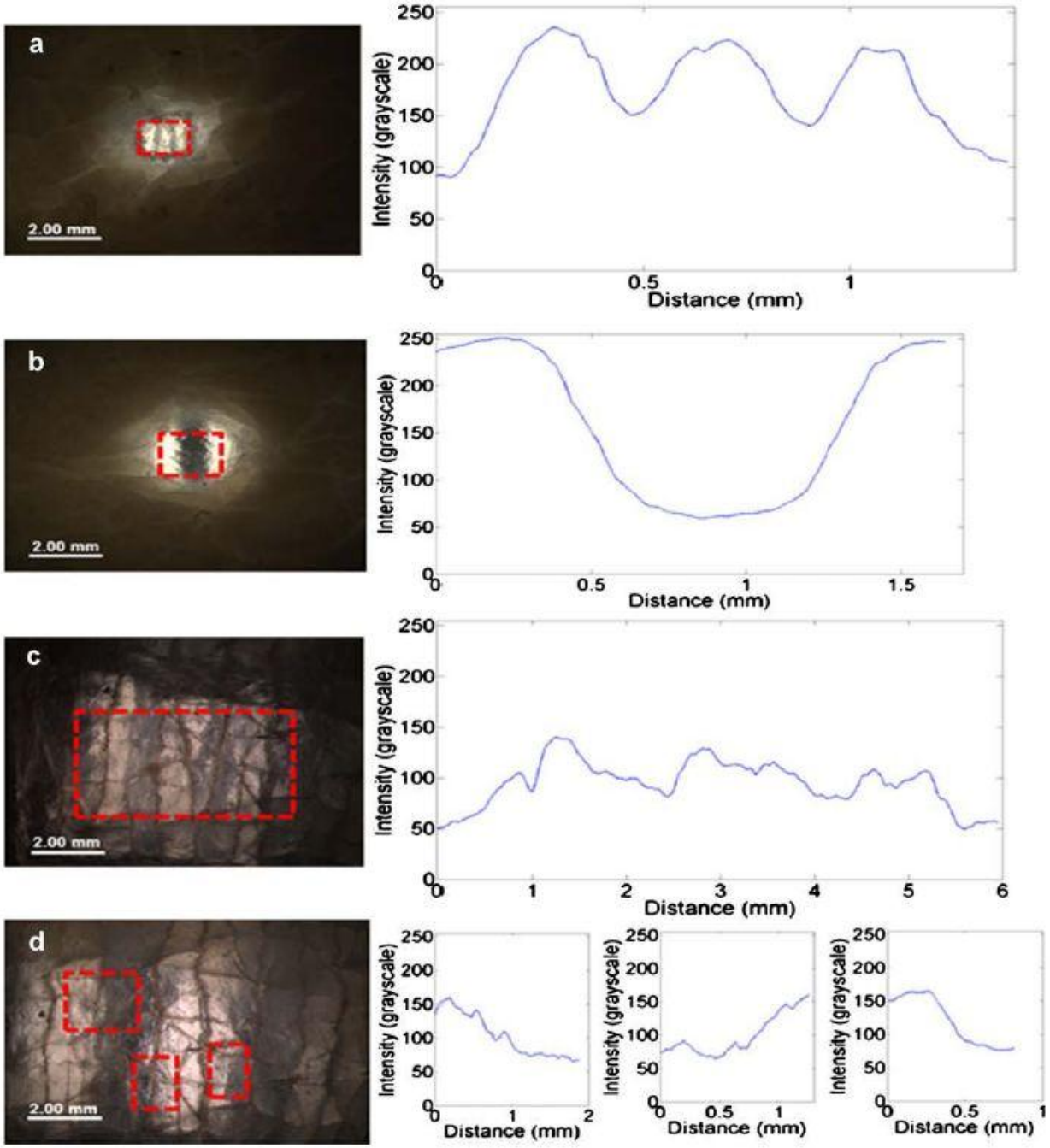

Figure 8. Representative images (ROI outlined in dashed boxes) and intensity plots for a) Group 1, Element 2 following 22 N compression using ROI Method 1, b) Group -1, Element 1 following 22 N compression using ROI Method 2, and c) Group -1, Element 2 following glycerol immersion using ROI Method 1, d) Group -2, Element 2 following glycerol immersion using ROI Method 2 [49]. Reprinted with permission from John Wiley & Sons Inc.

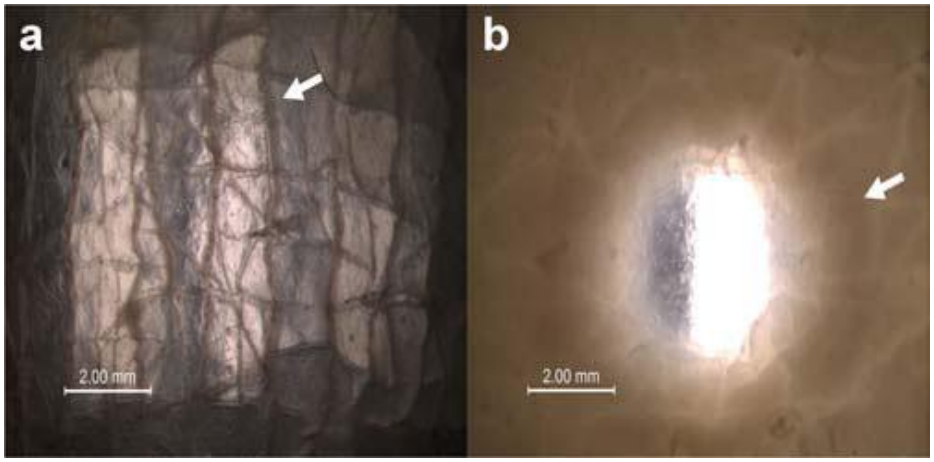

Figure 9. Differing morphologies of a: chemically cleared and b: mechanically cleared tissue specimens. White arrows indicate areas where structural modification is evident [49]. Reprinted with permission from John Wiley & Sons Inc.

In this same study, we wished to establish a correlation between tissue indentation and dynamic light transmission. To accomplish this, a thought experiment was proposed (see Figure 10): if we consider two tissue samples of different initial thicknesses, and the thicker sample is compressed to the same thickness as another thinner sample undergoing compression, will light transport through each sample be different? While tissue thinning will certainly result in increased transmission through compressed samples, we suspect that intrinsic optical property changes occur due to the deposition of mechanical energy into the solid and liquid components of the tissue. If stress relaxation tests were performed, where the thicker sample is indented in a ramp-hold displacement protocol to same final thickness as a thinner sample, what would happen? If light transmission changes during the hold phase at constant thickness, intrinsic changes must be occurring because the geometry is identical in both samples. We expected that the thicker sample would be more optically cleared than the thinner sample, resulting in increased light transmission, and that the light transmission would change over time while the sample underwent stress relaxation at constant final thickness. A combined mechanical/optical system for making force/displacement and light transmission measurements was developed as shown in Figure 11. This system consisted of a red continuous-mode laser source (optical power of 3 mW, spot size of 3 mm diameter) installed in the displacement cell of a BOSE Electroforce 3100 mechanical load frame. A load cell attached to the housing supporting the tissue sample measured applied indenter force, while a photodetector placed beneath the tissue sample recorded dynamic light transmission during indentation tests. Force and light transmission data shown in Figure 12 indicate that tissue indentation increased light transmission during the ramp

phase, most likely due to a combination of mechanical optical clearing and tissue thickness decrease. However, light transmission continues to increase during the stress relaxation phase, even though tissue thickness is held constant. This suggests that the intrinsic optical properties must be changing, since tissue geometry is fixed. Also, the degree to which dynamic light transmission increased during stress relaxation was found to be correlated with applied tissue strain (relative deformation).

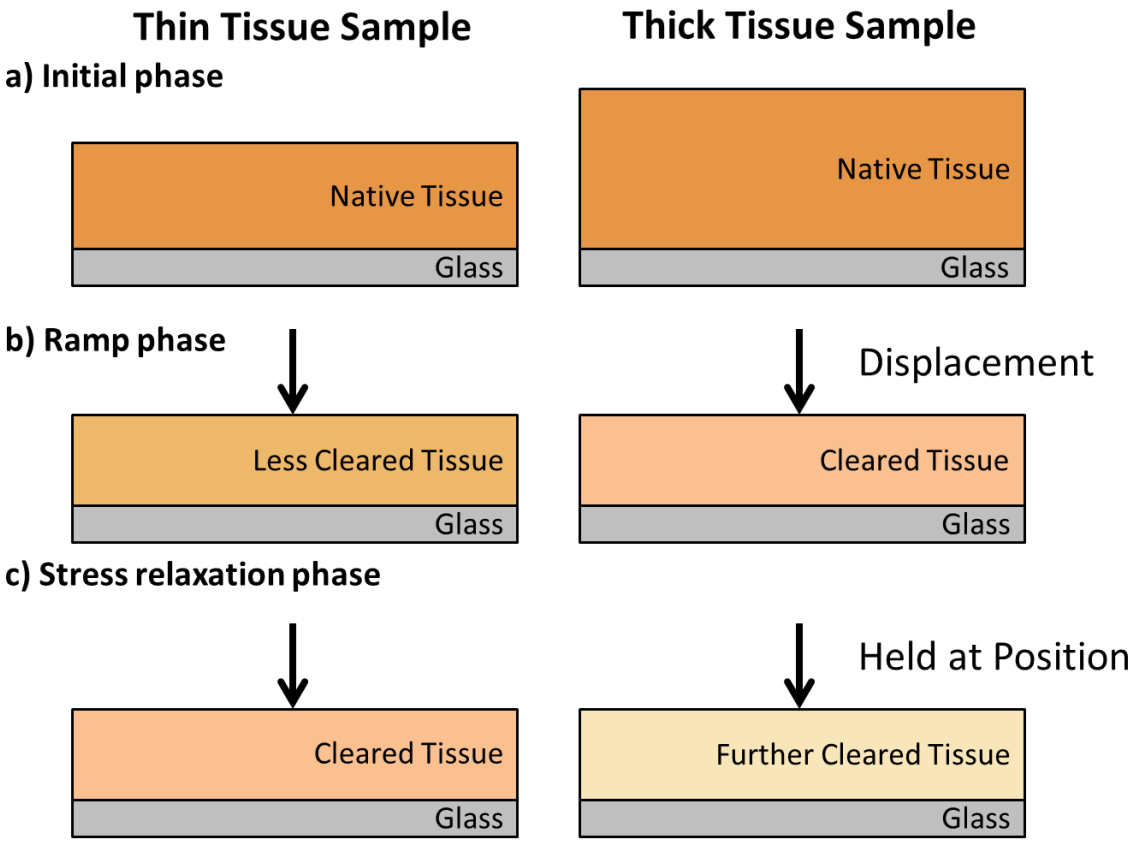

Figure 10. Thought experiment governing dynamic light transmission during stress relaxation. During the initial phase, samples are installed in the load frame. In the ramp phase, the indenter is displaced at a linear rate, compressing both samples to the same final thickness, which is expected to cause mechanical optical clearing. Lastly, during the stress relaxation phase the thickness of compressed samples is held fixed, and further optical clearing is expected.

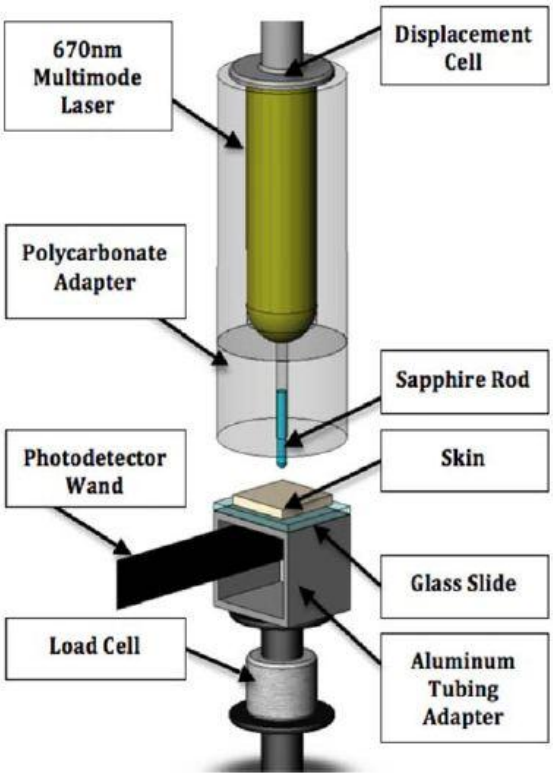

Figure 11. Compression experimental components. Optical power transmitted through porcine skin, applied load, and tissue thickness were recorded simultaneously [49]. Reprinted with permission from John Wiley & Sons Inc.

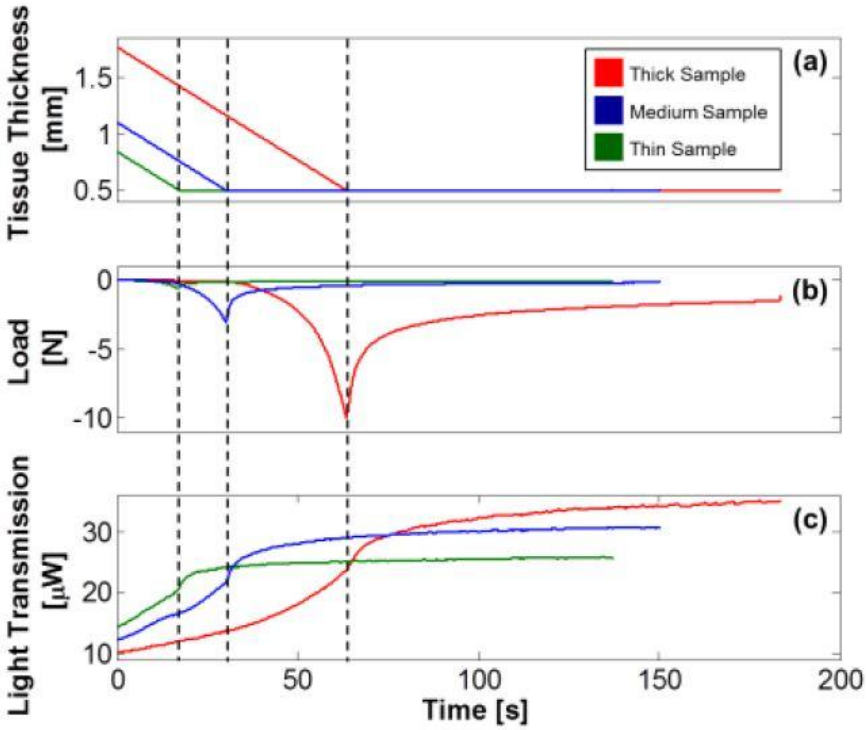

Figure 12. Dynamic plots of a: Tissue thickness, b: Compressive load, and c: Light transmission through representative localized compression specimens of various initial thicknesses. Note dynamic increases in light transmission during stress relaxation at constant final thickness [49]. Adapted with permission from John Wiley & Sons, Inc.

Modification of tissue optical properties by mechanical loading has been recently investigated by several groups. Askar'yan [50] demonstrated that local mechanical pressure results in deeper penetration of light in biological tissue. Research led by Agrba, Kirillin, and Kamensky [51, 52] recently demonstrated use of mechanical compression for image contrast enhancement and for tissue optical clearing to observe pathological changes in tissue [21]. Kirillin noted that compression caused dark regions to form in the OCT images and attributed this effect to interstitial or intracellular water flowing into the imaged tissue region. Chan *et al.* [53] and Shangguan *et al.* [54] have reported increased absorption and scattering coefficients when uniform pressure is applied over large tissue area (~100 mm^2) [24, 25]. These results differ from those of Askar'yan [50], Agrba *et al.* [21, 22], and Rylander [6, 45], but this is likely because these studies used uniform compression over a large area of tissue, while other works used local mechanical compression to induce smaller (~1 mm^2) compression zones, creating higher local pore pressure gradients within the tissue.

Chapter 3. Mathematical Modeling of Mechanical Optical Clearing

3.1 Introduction

Biological tissues are naturally turbid media due to refractive index mismatches between various tissue constituents, including proteins, cells, water, and blood [10-13]. This turbidity significantly reduces the efficacy of optical diagnostics and therapeutics. Tissue optical clearing is an emerging technique in which exogenous chemical agents are delivered to the tissue to reduce light scattering and absorption. One proposed mechanism of this effect is tissue dehydration, where such hydrophobic optical clearing chemical agents are used to displace interstitial water, changing local protein and water volume fractions and reducing index mismatching [55, 56]. Mechanical optical clearing is a recently developed technique in which mechanical force is used to reversibly and locally modify tissue optical properties, reducing light scattering and absorption. Our previous work has demonstrated that mechanical optical clearing of tissues results in increased light penetration depth [45, 46] as well as increased imaging resolution and contrast [57]. These effects are thought to be the result of reversible lateral water displacement caused by localized mechanical loading. As the tissue is indented or compressed, a pressure gradient develops within the tissue, driving interstitial water away from the compressed region.

This observed phenomenon is a complex interaction between the mechanical and optical domains of tissue response. As mechanical energy is transferred to the tissue, interstitial fluid transport is coupled to the mechanical response. The fluid transport, in turn, will modify the spatial distribution of tissue components, altering the optical properties *e.g.* absorption and scattering coefficients, resulting in enhanced light transport through the tissue. A fundamental understanding of the mechanisms of this effect is needed in order to guide further development of this technique for clinical applications. In addition, a computational framework is required in order to convert information from measured signals into information about intrinsic tissue properties, *e.g.* permeability or stiffness. From a previous study, we have observed that during "ramp-and-hold" stress relaxation tests, tissue light transmission increases as the tissue undergoes higher compressive strain (relative thickness change). However, when the level of strain is held constant, light transmission continues to increase even though tissue geometry is fixed, illustrating that additional mechanisms in addition to tissue thinning are present during

mechanical optical clearing. Another previous study demonstrated improved image quality using optical coherence tomography and imaging *in vivo* human and *ex vivo* porcine skin through a transparent indenter. Results showed that water volume fraction decreased as tissues were dehydrated in air, and that the measured increases in refractive index led to higher signal strength normalized to imaging depth. A previous modeling study demonstrated that moderate changes in scattering coefficient and refractive index could significantly increase light transmission even after taking into account transmission increases due to tissue thinning, but this model did not explicitly model the coupled behavior of fluid flow through a solid matrix.

In this study we propose a computational model of the mechanical optical clearing effect that combines computational modeling techniques from both mechanical and optical disciplines for investigating the underlying mechanisms of mechanical optical clearing (see Figure 13). In this model, we use a coupled mechanical poroviscoelastic model to simulate interstitial water transport caused by soft tissue deformation, then perform optical Monte Carlo simulation on the deformed tissue geometry to predict modified light transport. We will use this model to identify relationships between different material parameters and simulated output signals. Some inputs to the model will be provided from tissue characterization data, while other properties will be fitted to outputs from mechanical indentation experiments.

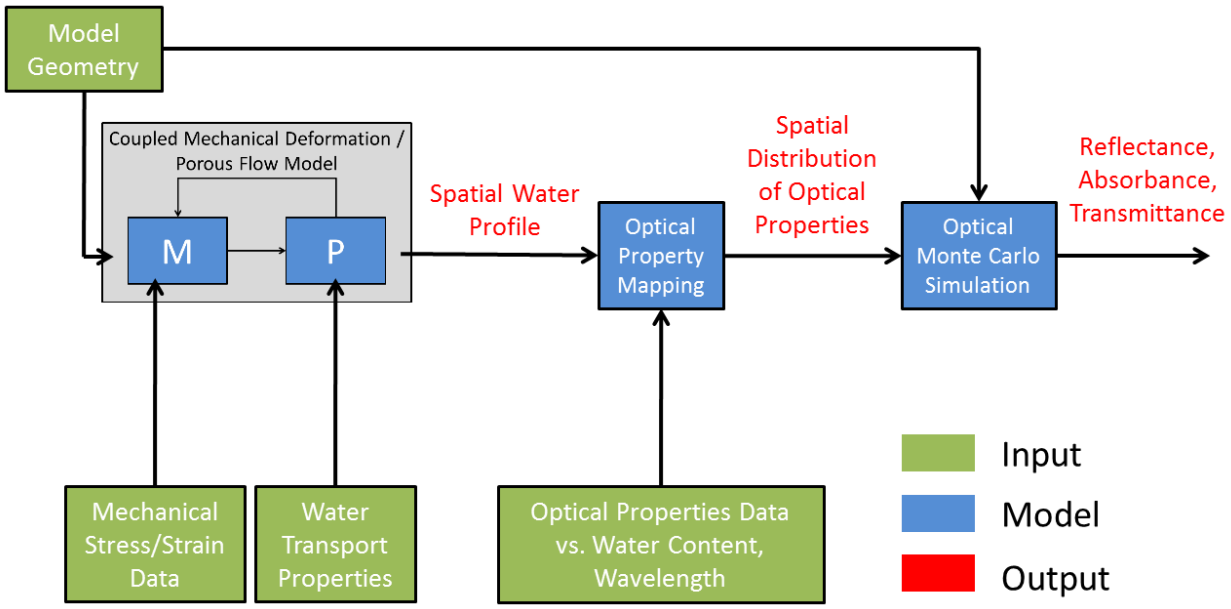

Figure 13. Computational model framework, denoting inputs, model components, and outputs.

3.2 Mechanical and Optical Tissue Characterization

Any mathematical model requires experimental data, both as input parameters and a means of validating predicted output signals. The proposed multi-domain framework requires data inputs from both mechanical and optical domains that will now be described in detail.

3.2.1 Hyperelastic Tissue Characterization

Soft tissues exhibit nonlinear elastic (hyperelastic) behavior and are thus capable of undergoing large deformations without failing. Most soft tissues can be approximated as having a two-phase stress/strain curve; the first phase is the 'toe region', where fibers in the tissue are randomly oriented and do not offer much resistance to deformation. However, as the tissue is further deformed, the fibers begin to align with each other, increasing tissue stiffness. Many models have been developed to capture this behavior, but the most common forms of the stress/strain relationship for soft tissue are the reduced polynomial and Ogden forms. The reduced polynomial form is written as

$$U = \sum_{i=1}^{N} C_{i0}(\bar{I}_1 - 3)^i + \sum_{i=1}^{N} \frac{1}{D_i}(J^{el} - 1)^{2i} \qquad \text{Eq. (8)}$$

And the Ogden form is given by

$$U = \sum_{i=1}^{N} \frac{2\mu_i}{\alpha_i^2}\left[\left(\frac{\lambda_1}{J^{\frac{1}{3}}}\right)^{\alpha_i} + \left(\frac{\lambda_2}{J^{\frac{1}{3}}}\right)^{\alpha_i} + \left(\frac{\lambda_3}{J^{\frac{1}{3}}}\right)^{\alpha_i} - 3\right] + \sum_{i=1}^{N} \frac{1}{D_i}(J-1)^{2i} \qquad \text{Eq. (9)}$$

where N is chosen in this study to be equal to 3, μ_i, α_i, and D_i are fitting parameters, λ_{1-3} are the orthogonal stretch ratios, and J is the total volume change [58]. The stretch ratios and volume change are automatically calculated by Abaqus from the data to be fit, and D_i is calculated from Poisson's ratio.

3.2.2 Viscoelastic Tissue Characterization

In addition to behaving as nonlinear elastic materials, soft tissues are also viscoelastic materials that undergo strain-rate-dependent changes in mechanical stiffness. The shear stress, T(t), is defined as the convolution of the shear strain rate, $\dot{\gamma}(t)$, shear relaxation modulus, $G(t)$, that may vary with time:

$$T(t) = \int_0^t G(t-s)\dot{\gamma}(s)ds \qquad \text{Eq. (10)}$$

where s is a dummy variable. A common way to represent the time-dependency of $G(t)$ is the Prony series, which defines a discrete time-dependent normalized shear relaxation modulus, $G_{norm}(t)$, as:

$$G_{norm}(t) = 1 - \sum_{j=1}^{N} g_j(1 - e^{-t/\tau_j}) \quad \text{Eq. (11)}$$

where N is chosen in this study to equal 3, and g_i and τ_i are material constants. In Abaqus, this is coupled to the hyperelastic constituent relationship by multiplying the parameters of the hyperelastic material law by $G(t)$. For the reduced polynomial form, this is written as

$$C_{i0,visco} = C_{i0}G(t) = C_{i0}\left(1 - \sum_{j=1}^{N} g_j(1 - e^{-t/\tau_j})\right) \quad \text{Eq. (12)}$$

and for the Ogden form this is written as

$$\mu_{i,visco} = \mu_i G(t) = \mu_i\left(1 - \sum_{j=1}^{N} g_j(1 - e^{-t/\tau_j})\right) \quad \text{Eq. (13)}$$

This is reasonable because the coefficients of the hyperelastic form are simply related to the initial (zero strain) shear modulus, G_0. For the reduced polynomial form (N=2),

$$G_0 = 2(C_{10}) \quad \text{Eq. (14)}$$

and for the Ogden form,

$$G_0 = \sum_{i=1}^{N} \mu_i \quad \text{Eq. (15)}$$

We performed stress relaxation experiments (N=8) using a 3-mm diameter hemispherical indenter. In stress relaxation tests, the tissue sample is deformed at some fixed strain rate to a specified strain, then held at that strain while the tissue relaxes, reorienting its fiber matrix to relieve the most stress. The calculated stress/strain data were normalized to the peak stress and entered into Abaqus.

3.2.3 Optical Tissue Characterization

One of the most important portions of the computational model is the conversion of local water volume fraction to intrinsic absorption and reduced scattering coefficients. To calculate tissue optical properties as a function of dehydration, *ex vivo* porcine skin specimens as

described in the previous section were cut into 20 mm x 50 mm strips and placed in a desiccator for zero, 2, or 6 hours (N = 5 for each dehydration time) in order to cause tissue water loss. Mass measurements before and after dehydration allowed estimation of the water loss by volume. Specimens were then placed sequentially at the front and back ports of an integrating sphere attached to a spectrophotometer (Cary 5000, Agilent Technologies, Santa Clara, CA), allowing for measurement of both diffuse transmittance and diffuse reflectance, respectively, over a spectral range of 400-1800 nm. Both measured signals were normalized to a NIST-traceable Spectralon reflectance standard (Spectralon SRS-99-020, Labsphere, Inc.; North Sutton, NH). To calculate optical absorption and reduced scattering coefficients from reflectance and transmittance data, the inverse adding-doubling (IAD) algorithm was used [59]. To use this method, we assumed the anisotropy factor, g , to be equal to 0.9 and the refractive index, n , to be equal to 1.38 at all wavelengths. Results are shown in Figure 14 . In order to input these data into Abaqus while the simulation was running, a Fortran subroutine was passed to the Abaqus simulation that calculated and wrote to file the optical properties as functions of the water volume fraction of each finite element for each data output request over time.

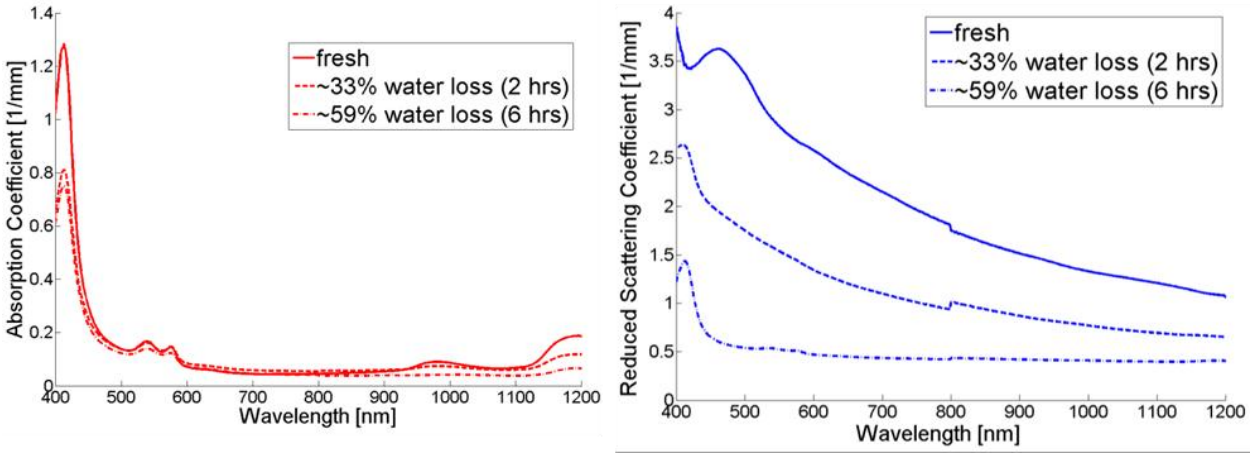

Figure 14. Calculated absorption and reduced scattering coefficients for different levels of dehydration.

3.3 Mechanical Finite Element Model

Biphasic poroelastic finite element (FE) models have been used broadly to characterize the mechanical behavior of hydrated soft tissues [60-65]. Such models describe coupled responses between a solid phase (*e.g.* extracellular matrix, collagen) and a liquid wetting phase (*e.g.* water). Abaqus (Simulia, Warwick, RI), a commercial FE software package, was used to

develop a biphasic mechanical finite element model of tissue indentation and the resulting mechanical response of both solid and liquid phases. This model is built by coupling a nonlinear elastic FE model and a model of the fluid transport through a porous medium [60]. The solid matrix is modeled as a hyperelastic, viscoelastic material with a fluid flowing through the pores of the solid structure. Flow for a wetting fluid through a porous medium may be modeled using Darcy's law for slow laminar flows driven by pore pressure gradients [66, 67]:

$$v = -\frac{k}{\rho g_G n_p}\nabla P \qquad \text{Eq. (16)}$$

where n_p is tissue porosity, v is the fluid velocity, k is the tissue hydraulic conductivity, ρ is fluid density, g_G is acceleration due to gravity, and ∇P is the interstitial pressure gradient. There are many effects that can change tissue hydraulic conductivity, but any effect that alters pore size and geometry will change the resistance to interstitial flow provided by the pores. Hydraulic conductivity is known to be highly nonlinear in articular cartilage [68], and its dependence on tissue deformation may be written as

$$k(e) = k_0 \exp\left(M\frac{e - e_0}{1 + e_0}\right) \qquad \text{Eq. (17)}$$

where e_0 is the initial void ratio, e is the current void ratio, k_0 is the initial hydraulic conductivity, and M is a tunable constant. We expect this nonlinear dependence on void ratio (and in turn tissue strain) to be critical to achieving good fidelity between the model and mechanical datasets because of large compressive deformations. In this study we do not experimentally determine the hydraulic conductivity, but leave it as a part of the parameter set to be fitted in an optimization routine.

One of the outputs of this biphasic FE model is the spatial water distribution over time within the biphasic tissue. Because the water volume fraction varies in space and time, the optical properties should also vary as a function of the water fraction. To implement this relationship, we use a simple look-up table approach. We performed optical property measurements (described in the experimental data section) for skin samples undergoing different degrees of dehydration over a large spectral range, allowing for selection of an interpolant for optical properties specific to a chosen wavelength. The distribution of optical properties in space and time could then be input to Monte Carlo simulations.

In this study, the mechanical biphasic model will be used to simulate ramp-and-hold stress relaxation experiments using indentation-mode deformation. The geometry and boundary

conditions of the mechanical simulations performed are shown in Figure 15. The bottom of the skin sample was fixed, and no pore flow was permitted across any outer edge of the mesh. A rigid nonporous indenter was constrained to compress the deformable skin sample to 50% bulk compressive strain at a strain rate of 0.1 sec^{-1}, then held in place as the sample underwent stress relaxation. The indenter/sample interface was assumed to be frictionless.

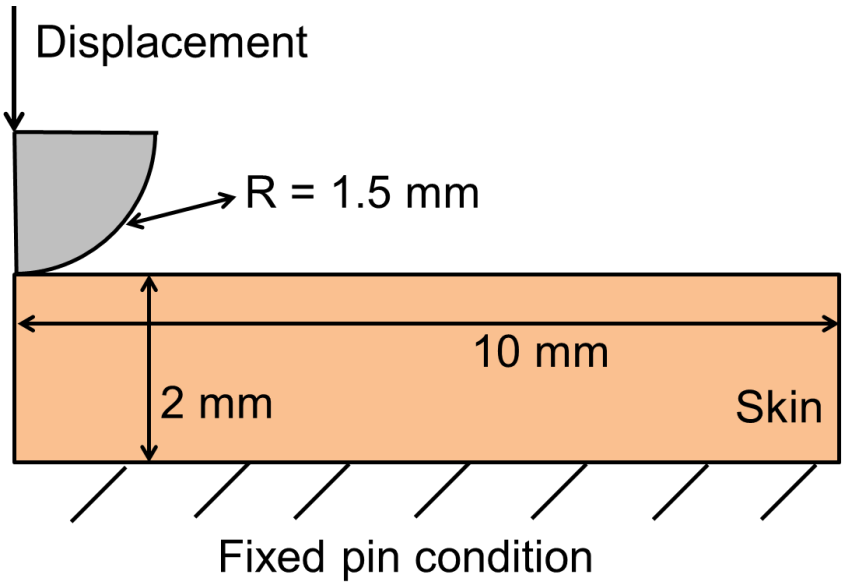

Figure 15. Configuration for finite element simulation of stress relaxation experiments.

3.4 Optical Monte Carlo Simulation

Optical simulation of biological tissues is most commonly performed using Monte Carlo (MC) simulation [69]. These methods typically assume the particle model of light, where photons travel along rays through the simulated medium. Monte Carlo methods also assume that optical wave effects such as interference may be ignored. Monte Carlo methods are stochastic in nature; a large number of photons are launched randomly through a mesh of elements or voxels, with physical laws for reflection, refraction, scattering, and absorption determining each photon's path. Light transport through tissues is governed by the radiative transport equation (or Boltzmann transport equation for general electromagnetic particles). However, analytical solutions of the radiative transfer equation are usually impossible for realisticly complex models and boundary conditions due to the large number of independent variables to be solved [70]. The diffusion approximation (assumption that photons follow diffusion-like behavior) makes analytical solution more feasible, and biological tissues are well modeled by this assumption due to their high ratio of scattering to absorption behavior. Compared with analytical solutions, MC

methods offer lower computational cost and simpler inclusion of multiple boundary conditions compared with analytical methods [70]. For sufficiently large numbers of photons, Monte Carlo simulation outputs converge to an accurate description of photon transport in turbid, diffuse, and heterogeneous media such as biological tissues [71].

Given spatial distributions of optical properties predicted by Abaqus, optical MV simulation could be performed accounting for these fully heterogeneous media. We chose to use TIM-OS, an open-source MC simulator developed by Shen and Wang [72]. TIM-OS is designed to efficiently run MC simulations on 3D meshes of tetrahedral elements, where each individual element may have its own optical properties. Figure 16 shows the boundary conditions for these simulations, and tabref provides optical properties for each material region (note that skin optical properties will change over time slices due to optical clearing effects). The geometry of the indented tissue sample was extended such that no more than 5% of photons exited out the side of the mesh. Each run simulated 10^8 photons traversing the mesh, which contained on average ~400,000-500,000 elements.

Because TIM-OS only performs 3D (tetrahedral) simulations, but FE simulations were modeled in 2D (with rectangular axisymmetric elements), the geometry and outputs of each FE solution needed to be mapped to a new 3D mesh. Custom code was written in Matlab (The Mathworks, Natick, MA) to read the 2D geometry of the indented tissue and write a Python script to be fed to the Abaqus GUI. This Python script would then command Abaqus to generate a 3D tetrahedral mesh from the deformed 2D rectangular FE mesh. The 2D radial distribution of varying optical properties in the skin sample was used to generate a 3D interpolation space based on a Delaunay triangulation in Matlab. The code then assigned each tetrahedron optical properties based on the position of the element's centroid relative to the axis of symmetry about the indenter at each point in time. If the element centroid was located outside the region of significant optical clearing (>0.5%), it was assigned the baseline (initial) optical properties.

We are interested in the temporal dynamics of mechanical optical clearing, and since the mechanical finite element model provides output over time, it would be desirable to have optical MC simulations performed at each point in time. Since the dynamics of mechanical optical clearing are very slow compared to the speed of light, each MC simulation is a steady-state simulation. If we use a steady-state MC simulation at each time frame we request output from the mechanical model, a multiframe snapshot of the optical response over time can be predicted

and overlaid with mechanical results. To accomplish this, code was written in Matlab to read the mechanical FE output mesh geometry and optical property distributions for each time point of interest. After MC simulation, Matlab was used to process each time frame of optical outputs and calculate percentages of photons that were transmitted through the bottom of the glass slide (transmittance), reflected through the top of the glass indenter (reflectance), or absorbed by the tissue (absorbance).

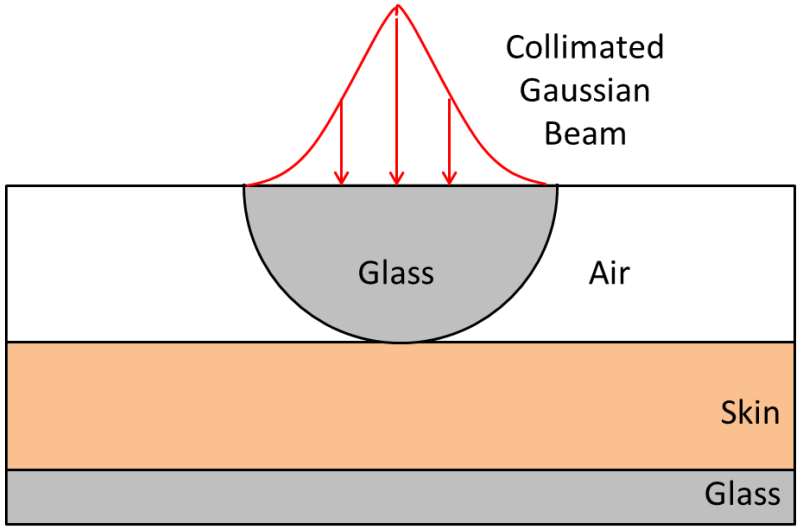

Figure 16. Geometry of MC simulations, shown in the initial time frame corresponding to the first frame of mechanical simulations. Skin contains varying optical property distributions, glass and air have fixed properties.

Table 2. Optical properties for material regions in MC simulations. Note that skin values for absorption and scattering coefficients will change during simulations based on water transport from FE models.

Region	μ_a [mm^{-1}]	μ_s' [mm^{-1}]	n [-]
Skin (baseline)	0.064	2.40	1.38
Glass	0.001	0.001	1.5
Air	0.001	0.001	1.0

3.5 Results

3.5.1 Parametric Study of Nonlinear Poroelastic Model

In order to better understand the mechanical model, a parameter study was performed on a nonlinear poroelastic model of hemispherical indentation. In this model, porcine skin was modeled as a hyperelastic porous medium, where the solid matrix is assumed to not be viscoelastic. This reduces the parameters to the nonlinear stiffness, E(e), hydraulic conductivity, *k*, and Poisson's ratio, *v*, and the initial tissue porosity (fixed as 70%). For this parameter study we chose to fit a hyperelastic material law to measured stress/strain data, leaving *k* and *v* to be varied. To collect hyperelastic characterization data, a BOSE Electroforce mechanical load frame

(BOSE, Eden Prairie, MN) was used to perform uniaxial indentation on *ex vivo* porcine skin samples using a flat-tipped, glass, 3 mm-diameter indenter. Tissue load and displacement were measured and used to calculate stress and strain. Specimens (N = 5) were indented to 50% compressive strain at a rate of 0.02 mm/s. Once the stress/strain data was acquired, Abaqus was used to fit a 3-term Ogden model to the data. In this parametric study, Poisson's ratio was set to 0.2, 0.3, or 0.4.

Table 3 shows fitted Ogden parameters for different values of Poisson's ratio, demonstrating that Poisson's ratio only affects D_i, and that the other portion of the Ogden model is unchanging over the parameter study. Figure 14 shows the calculated optical properties to be used as the look-up mapping. The decreased absorption at infrared wavelengths is indicative of water loss, and scattering decreases with both wavelength and tissue dehydration as expected. Discontinuities at 800 nm are the result of detector change when scanning large spectral ranges. With these data, the model could be executed for the parametric study described previously.

Water transport through the porous medium is defined in terms of the permeability, k [m/s], and porosity, p [%]. For parametric study, k was set to 4e-8, 4e-9, or 4e-10 m/s. Porosity, the fraction of void volume to total tissue volume, was assumed to be 70% since the fractional volume that is not filled with solid protein matrix will be mostly water, which is approximately 70% of skin tissue by volume [73].

Table 3. Fitted Ogden hyperelastic model for various values of Poisson's ratio.

			ν		
			0.2	0.3	0.4
i	μ_i [MPa]*	α_i [-]*	D_i [MPa^{-1}]	D_i [MPa^{-1}]	D_i [MPa^{-1}]
1	0.672	0.765	20.4	12.6	5.83
2	0.0391	7.67	0.0	0.0	0.00
3	-0.638	0.0922	0.0	0.0	0.00

* independent of ν

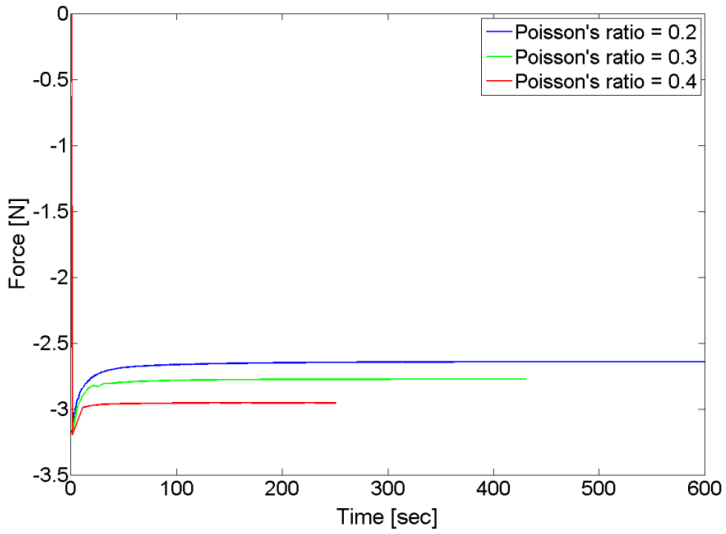

Figure 17. Representative force relaxation curves for k = 4 x 10^{-8} m/s. Curves are of different length because steady state was reached more quickly for higher Poisson's ratio, terminating the simulation.

Figure 17 shows representative force relaxation curves for three different values of Poisson's ratio with a fixed permeability of 4 x 10^{-8} m/s. It is evident from these data that the force relaxation may follow an exponential decay. To evaluate this effect, we calculated the apparent time constant, τ_F through an exponential fit of force data after the maximum value as summarized in Table 4. To determine the influence of mechanical properties on τ_F, we plotted τ_F as a function of both *k* and *v* for each permutation of values as shown in Figure 18. For each fixed permeability value, τ_F was seen to linearly decrease with increasing Poisson's ratio, while in fixed Poisson's ratio cases τ_F followed a power law, decreasing dramatically with increased permeability. Because the values of τ_F vary widely between these parameter sets, we compared the fitted parameters by normalizing them to the mean of the fitted data.

Table 4. Force time constants from nonlinear regression. All coefficients of determination exceeded 0.98.

Table for τ_F [sec]	*v*		
k [m/s]	0.2	0.3	0.4
4e-8	1.86	1.18	0.755
4e-9	14.1	8.76	5.29
4e-10	85.8	65.1	35.6

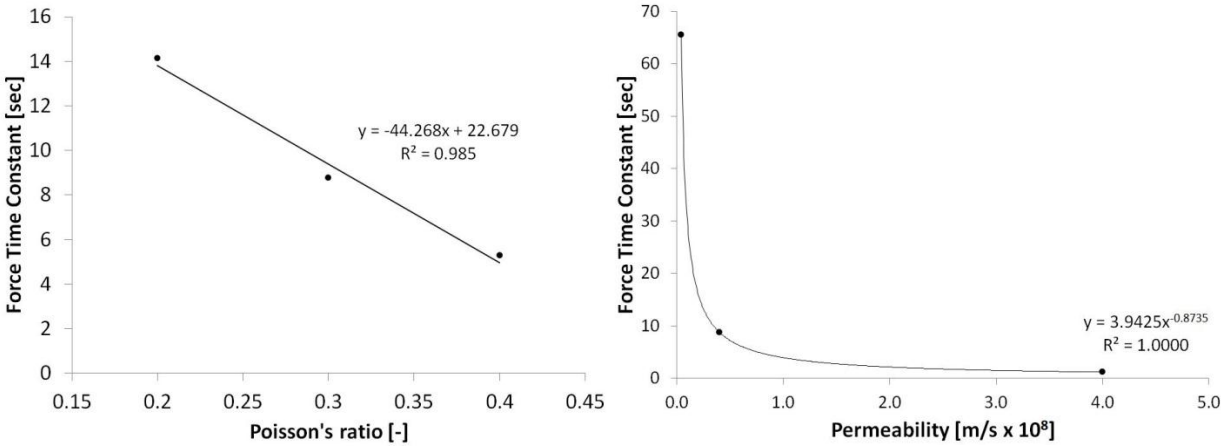

Figure 18. Time constants as functions of mechanical parameters for a) fixed k = 4 x 10^{-9} m/s, and b) fixed ν = 0.3.

In addition to parameterizing the intrinsic tissue properties, we also varied indenter geometry in order to study changes to the distribution of optical properties. Figure 19 shows steady-state reduced scattering coefficient distributions using the poroelastic model with k = 4e-8 m/s, ν = 0.3. The predicted optical clearing regions in Figure 19 match observed changes in optical properties, with hemispherical indenters producing darker recessed tissue close to the indenter axis, and flat indenters having the greatest optical clearing at the brim of the indenter. Figure 20 compares optical clearing efficacy before and after a stress relaxation period. Results show increased change in water distribution and optical property distribution over the relaxation period. Interestingly, the model predicts water accumulation outside the indented tissue region in the most superficial layers, an effect observed in previous work [49]. In Figure 21 a similar trend is observed, where the depth-averaged water volume fraction increases about initial value outside of the cleared region. The increase in depth-averaged reduced scattering coefficient means that the area of water accumulation will appear more turbid, matching experimental observations. Optical fluence through a 2D slice of the 3D optical mesh was extracted from Monte Carlo simulations as shown in Figure 22, indicating the classic radial diffusion pattern in both geometries. Hemispherical indenters creating focusing a short distance from the tip of the indenter, while flat indenters created a more uniform fluence distribution in the tissue.

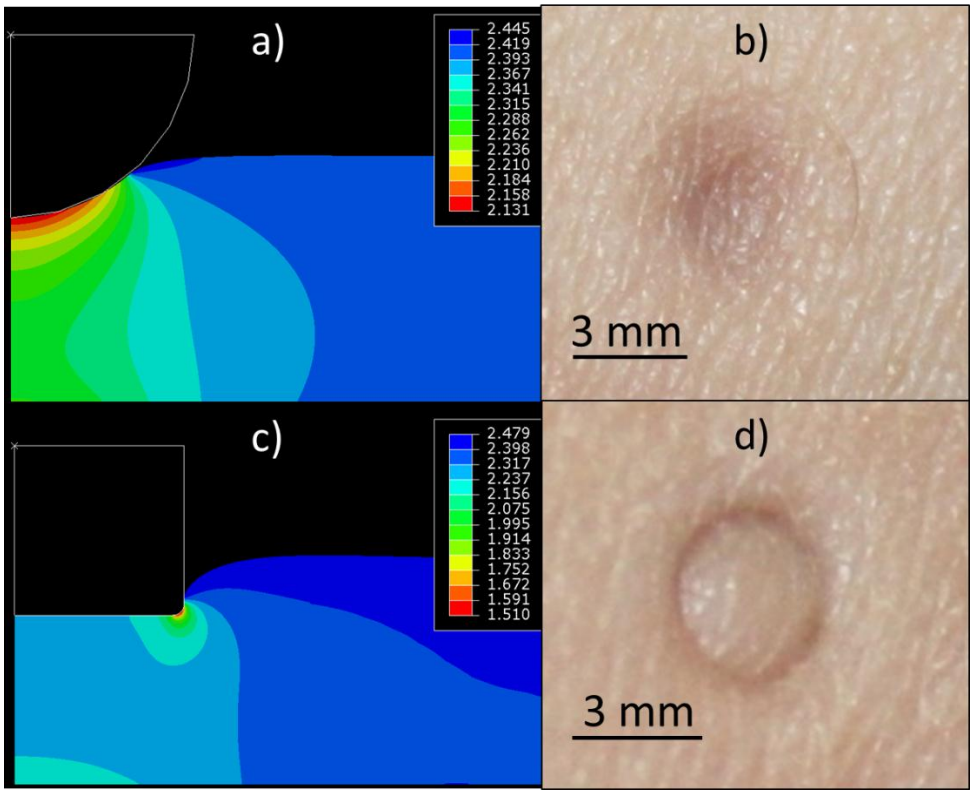

Figure 19. Reduced scattering coefficient results [mm^{-1}] for indentation to 25% bulk compressive strain with ν = 0.3, k = 4e-9 m/s. Simulations were performed for both a) hemispherical and b) flat indenters, each with a 3 mm diameter. Optical clearing profiles are compared to *in vivo* indentation using c) round and d) flat indenters of the same diameter.

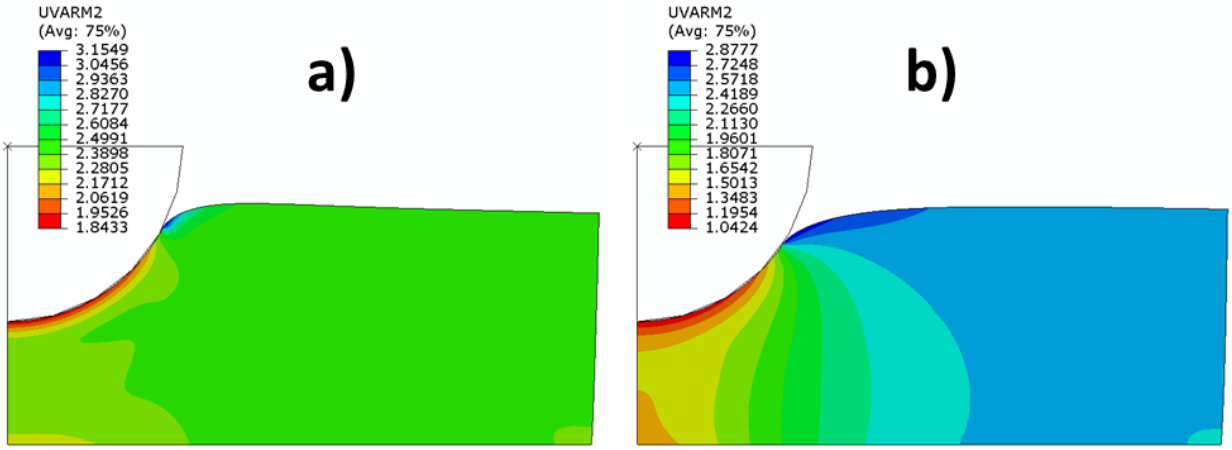

Figure 20. Example of transient changes in reduced scattering coefficient for ν = 0.2, k = 4e-8 m/s a) after indentation and b) at steady state. Note the water accumulation region (dark blue), which relaxes during the dwell period but increases in size.

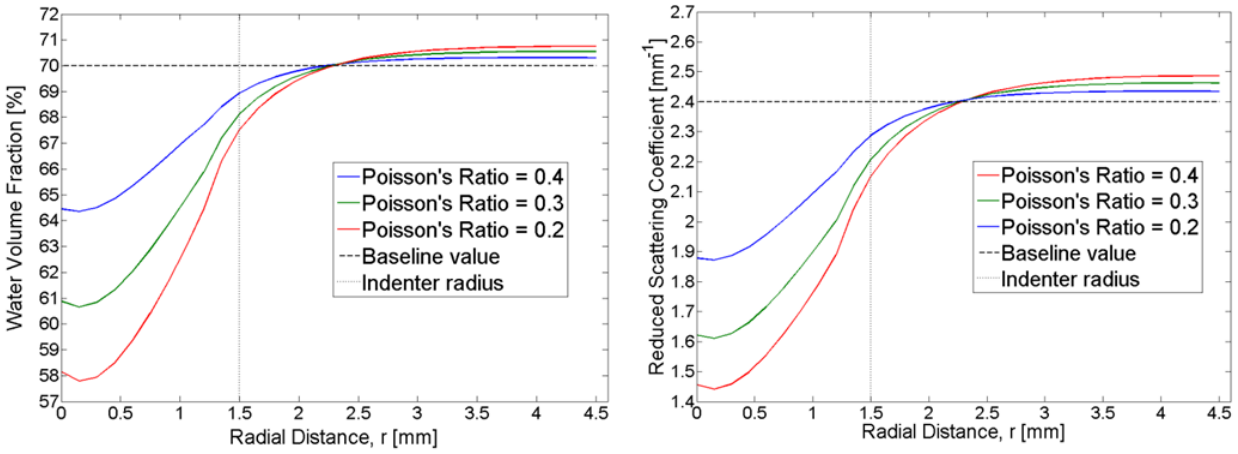

Figure 21. Depth-averaged a) water volume fraction, and b) reduced scattering coefficient for different values of Poisson's ratio. Dotted line indicates initial value. Note that away from the indenter, the water volume fraction and scattering coefficient slightly increase, suggesting water accumulation.

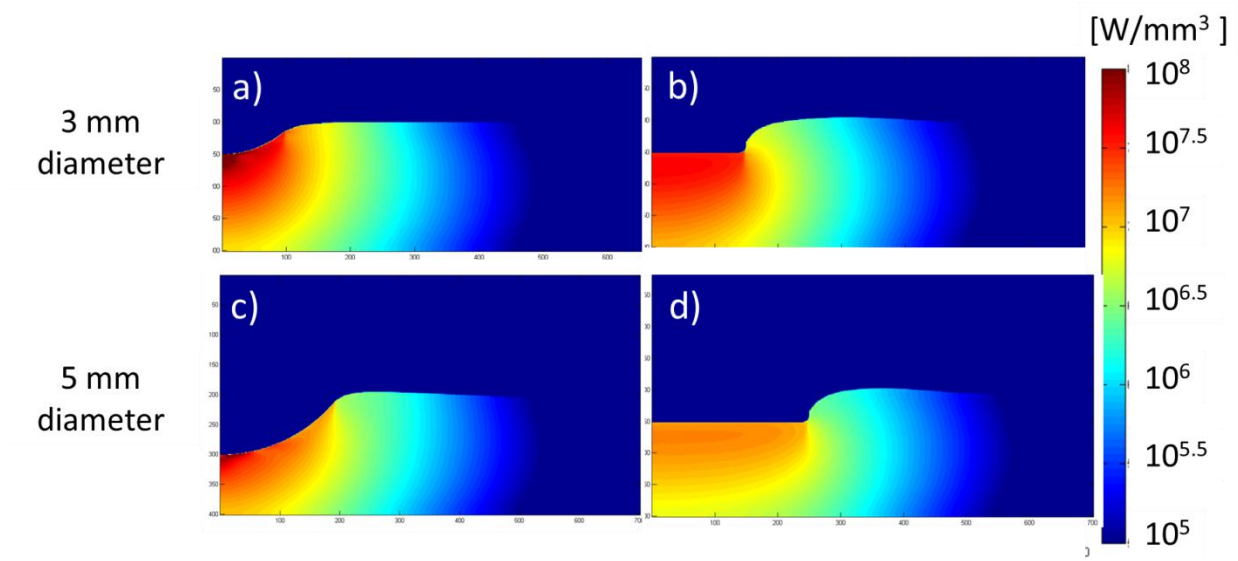

Figure 22. Simulated optical fluence for a variety of indenter geometries, including a) 3 mm hemispherical, b) 3 mm flat, c) 5 mm hemispherical, and d) 5 mm flat.

3.5.2 Fitting of Poroviscoelastic Model

In this section, we add viscoelasticity to the material properties of the simulated skin samples in order to more accurately predict tissue relaxation and optical clearing. However, because this model has many unknown material parameters (6 viscoelastic parameters, 2 hydraulic conductivity parameters) we performed an optimization routine using Matlab. Matlab would generate an Abaqus job script to solve a model, then Matlab would take the solution and compare it against experimental force data. Using the Nelder-Mead simplex optimization algorithms available in Matlab, predicted applied force was fit to data acquired from uniaxial compression stress relaxation tests. In these tests, 15-mm diameter discs of skin were

compressed to 25% compressive strain and held for 1,000 sec. As shown in Figure 23, the optimization routine found a good fit to the mean force response curve. It was evident from multiple executions of the routine that the use of nonlinear hydraulic conductivity was crucial for achieving the best fit. Optical transmission data reproduced dynamic trends observed in the data, but generally with high DC offsets. After normalizing each transmission curve to its initial value, the error between model output and data is significantly reduced.

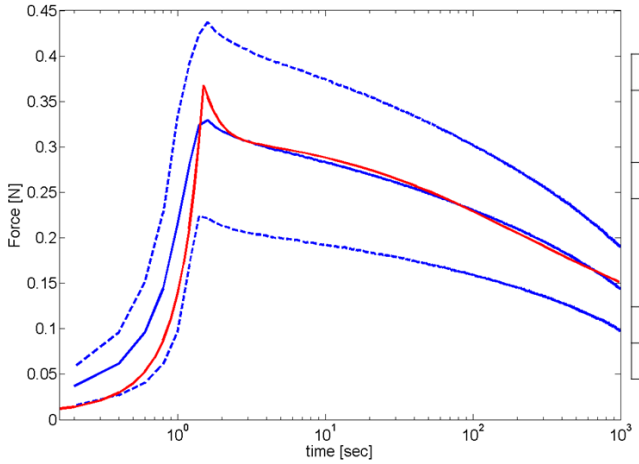

Hyperelastic	i	C_{i0} [Pa]	D_i [Pa^{-1}]
	1	1193.83	6.2822e-4
	2	26803.46	0
Viscoelastic	**i**	**g_i [-]**	**τ_i [sec]**
	1	0.2998	0.3932
	2	0.01063	10.374
	3	3.06e-4	726.52
Porous Medium	**k_0 [m/s]**	**M [-]**	**v [-]**
	5×10^{-8}	24.756	0.2

Figure 23. Optimized model fit to uniaxial stress relaxation force data (N=8). Table lists values of fitted parameters.

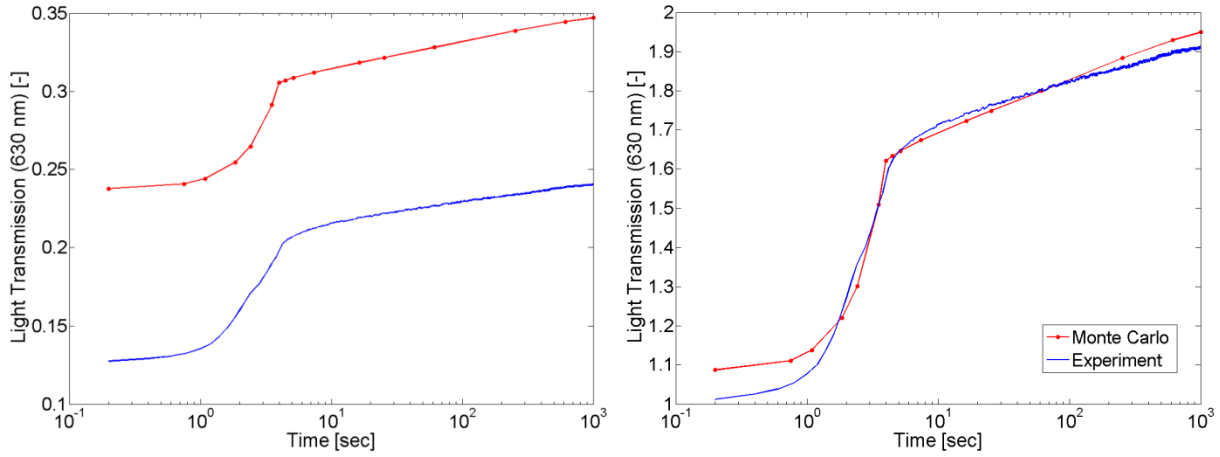

Figure 24. Optical transmission predicted for one skin sample. Predicted optical output based on mechanical model fit to individual skin sample's data (see Figure 23).

3.6 Discussion and Conclusions

There are several areas where the model could be expanded to improve accuracy in predicting mechanical optical clearing effects. For this study we did not input data to describe changes in refractive index, but instead assumed refractive index was fixed. This assumption was made because optical property calculation using IAD was performed for two sets of data, diffuse reflectance and transmittance, allowing for fitting of absorption coefficient and reduced

scattering coefficient, but not refractive index. Our previous modeling study suggested that refractive index was an important parameter determining optical clearing efficacy [74], and we have recently determined a relationship between bulk refractive index and water volume fraction at 1310 nm [48]. In the future, this effect can be incorporated into future models. Finally, we assumed isotropic mechanical behavior for porcine skin due to a limited mechanical dataset, but skin is known to be a highly planar, anisotropic tissue. Future work may include performing mechanical tests in different deformation modes to create a more complete description of tissue mechanical responses, as well as investigating the likely anisotropic nature of hydraulic conductivity of skin. This would provide enough data to fit parameters of a transverse isotropic model for skin tissue, such as the Fung or Holzapfel models [75].

This model demonstrates a novel tool for examining the intersection of tissue biomechanics and biomedical optics. Comparison between model outputs and coupled mechanical and optical experimental data suggest that optical property change through interstitial water movement is a valid potential mechanism for mechanical optical clearing. Through further refinement, this model can be used to perform optimization of mechanical optical clearing devices.

Chapter 4. Applications in Diffuse Reflectance Spectroscopy

4.1 Introduction

Light-based diagnostic and therapeutic procedures are severely limited by the penetration depth of light in tissue. Biological tissues are heterogeneous materials primarily composed of cells, water, and proteins; spatial variations in tissue refractive index induce multiple scattering of incident light [12, 16, 53, 76]. This turbidity reduces the energy delivered to deep target tissue regions. A significant amount of research has been devoted to the development of "tissue optical clearing" techniques that aim to overcome the limitations caused by this natural tissue-light interaction. Such techniques modify tissue optical properties in order to increase delivery of light deeper into turbid tissues. One potential mechanism of optical clearing is tissue dehydration due to water displacement [6, 10, 12, 13, 16, 22, 24, 33, 45, 46, 56]. Mechanical optical clearing is a recently developed technique that maintains stratum corneum integrity, creates localized effects, and may exhibit fast rates of optical clearing [13, 45, 46]. Mechanical optical clearing is achieved by locally compressing tissue and is thought to result from interstitial water and blood displacement, leading to local tissue dehydration and altered tissue scattering and absorption [6, 45, 46]. As tissue is compressed, water and blood are displaced laterally from regions undergoing high compressive strain (relative thickness change), decreasing local water volume fraction and thus reducing refractive index mismatch between constituents and lowering scattering and absorption. A previous Monte Carlo study has indicated that increases in transmission due to tissue thinning alone are not high enough to match experimentally observed light transmission increases during localized compression [74].

Mechanical optical clearing has been shown to increase imaging resolution and contrast [48, 77], as well as light transmission through *ex vivo* porcine skin [46, 77]. However, a fundamental understanding of resultant changes in intrinsic tissue optical properties during mechanical indentation is needed. Quantifying changes in optical properties using diffuse reflectance spectroscopy (DRS) would greatly add to our understanding of mechanical optical clearing techniques. DRS is a minimally-invasive technique that allows optical detection of physiological changes in tissue through wavelength-dependent measurements of backreflected light. Measured spectra are typically analyzed with computational models and inverse look-up table approaches in order to extract tissue optical properties including absorption and reduced

scattering coefficients [78-82]. Fiberoptic DRS measurements are obtained by illuminating tissue with broadband light through an emitting optical fiber contained within a probe, usually in contact with the tissue. Light remitted from the tissue is collected by an adjacent collecting fiber and analyzed by a spectrometer to generate a diffuse reflectance spectrum (see Figure 25). However, many researchers have observed that applied probe pressure during indentation can affect tissue optical responses and properties [78, 83-87].

The goal of this study was to investigate the effects of localized mechanical indentation, particularly during transient stress relaxation, on the optical properties of *ex vivo* porcine skin. Our previous work has described the thickness-independent optical clearing effects of indentation on *ex vivo* porcine skin specimens [77]. Increased light transmission was found to correlate with tissue strain during indentation, with greater compressive strain resulting in greater light transmission increase. More importantly, light transmission continued to increase while holding the tissue in compression at constant thickness, indicating that mechanisms other than tissue thinning affected tissue light transmission. But these experiments were incapable of determining the optical properties of the tissue and how these properties were dynamically modified. This study explored the dynamic effects of different indentation depths on tissue optical properties. Diffuse reflectance spectra of *ex vivo* porcine skin specimens were obtained during displacement-controlled compression. Tissue thickness, load, light transmission, and diffuse reflectance spectra were simultaneously recorded during indentation and tissue optical properties were extracted from the diffuse reflectance spectra using a previously described inverse look-up table (LUT) model [79, 82]. We hypothesize that localized compression will induce local optical clearing effects (*e.g.* water transport) in the tissue, resulting in a reduction in reduced scattering coefficient.

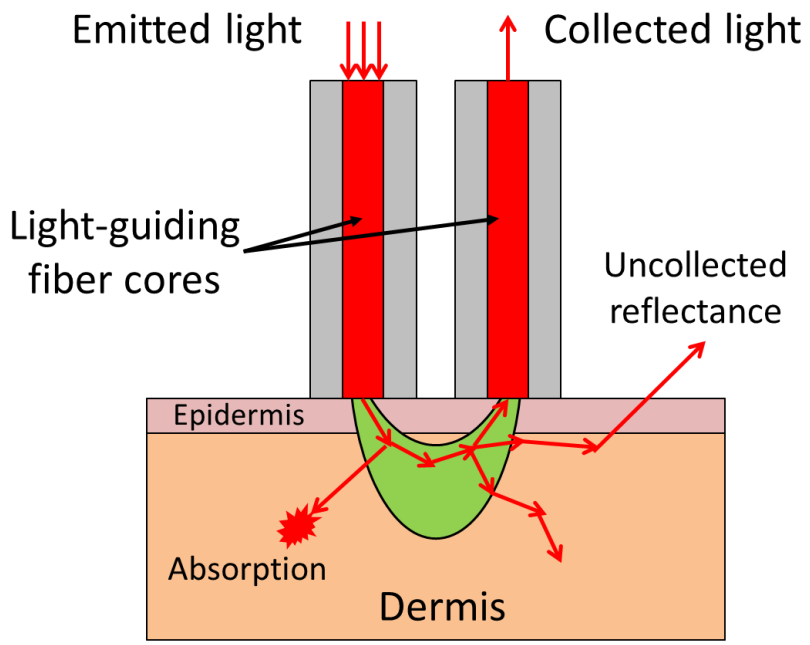

Figure 25. Schematic of principles of DRS, showing a simple two-fiber configuration. Those photons that reach the collecting fiber have traveled through the 'banana-shaped' sensing volume (green).

4.2 Methods

4.2.1 DRS System

A custom-built diffuse reflectance spectroscopy system (Figure 26a) was used to collect diffuse reflectance spectra from *ex vivo* porcine skin specimens during dynamic compression tests. Broadband light from a tungsten halogen lamp (Ocean Optics LS 1; Dunedin, FL) was delivered to the tissue via an emitting optical fiber within a custom fiberoptic probe. A collecting fiber adjacent to the emitting fiber collected remitted light and delivered it to a UV-VIS spectrometer with a range of 350-1000 nm and spectral resolution of 1.5 nm at FWHM (Ocean Optics USB 2000+). The custom DRS probe built for this study was designed 1) to illuminate the tissue and collect remitted light for reflectance spectra measurements, and 2) to indent tissue specimens. The fiber probe consisted of two adjacent multimode silica fibers (Thorlabs BFH-22-200, NA = 0.22, 200 µm core diameter, 400 µm cladding diameter, Newton, NJ) placed within a flat-tipped 18 gauge hypodermic needle (0.838 mm inner diameter, 1.27 mm outer diameter) as shown in Figure 26b. Fibers were epoxy-bonded within the hypodermic needle and syringe using EP30 (Masterbond, Hackensack, NJ), resulting in a center-to-center source-detection separation of ~400 µm. The fibers and hypodermic needle were polished flat at the tip and connectorized

with SMA connectors at the proximal end. The distal end of the fiber probe had a flat, circular surface area of 1.27 mm^2.

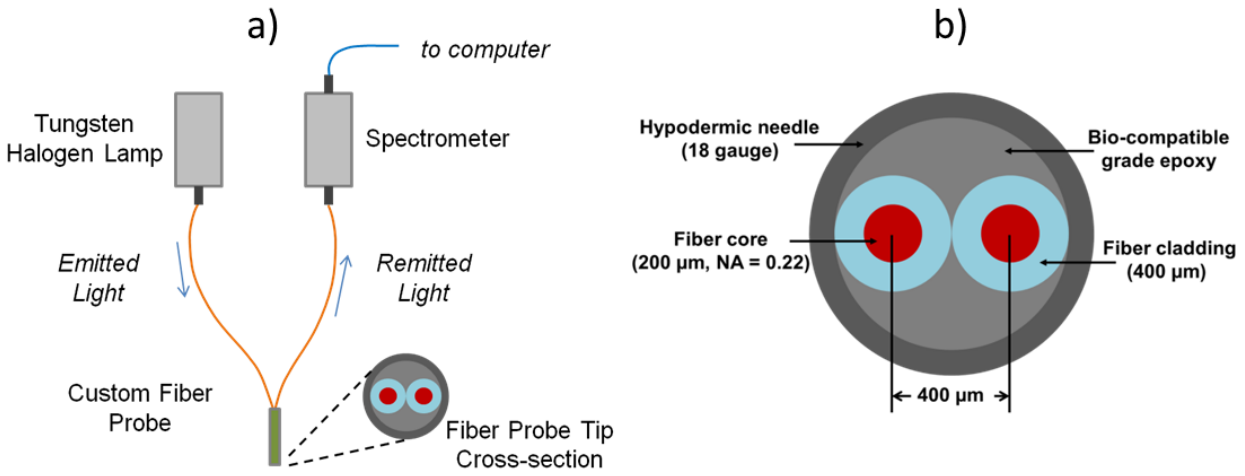

Figure 26. DRS system configuration. DRS probe cross section, showing fiber separation distance.

4.2.2 Tissue Sample Preparation

Ex vivo porcine skin specimens were obtained from a local abattoir and were prepared by removing the adipose layer by dissection with a scalpel. After being trimmed to 2 cm x 2 cm squares, specimens were stored for no more than 5 hours at 4 ºC in phosphate buffered saline moistened wraps prior to experimentation. Specimens were allowed to equilibrate to room temperature for 30 minutes prior to testing. Initial thickness was calculated from measured displacement during testing.

4.2.3 Boundary Conditions for DRS During Indentation

DRS probes interrogate a finite depth into tissues, and this depth is a function of the separation distance between the two fibers. However, the light reaching the collection fiber must not have interacted with the bottom surface of the tissue sample in order to satisfy the semi-infinite boundary condition. The minimum tissue thickness required to ensure the semi-infinite boundary condition was measured by placing a piece of white paper beneath the tissue sample during indentation to various thicknesses and recording when the DRS signal intensity changed more than 5%. We determined that our probe was sensitive to the boundary surface beneath a planar tissue specimen if the tissue was indented beyond a final thickness of ~0.8 mm. To avoid this error, indentation tests were performed on specimens consisting of two epidermal/dermal

skin samples stacked on top of each other such that the epidermis of the top sample was facing up and that of the bottom sample was facing down. This stacked specimen results in a dermal layer with doubled thickness, satisfying the semi-infinite medium condition that is required for DRS analysis and optical property calculation [88]. Stacked specimens were compressed to final thicknesses of no less than 1.0 mm, which allowed study of high tissue strains but still satisfied the assumption of a semi-infinite boundary condition.

4.2.4 Combined Mechanical/Optical System

The DRS probe was designed to interface with a BOSE® ElectroForce® 3100 mechanical load frame (BOSE, Eden Prairie, MN). This load frame has a displacement resolution of 1.5 microns over a 5 mm stroke and a force resolution of 6 mN with a 22 N capacity load cell, which provides satisfactory displacement, load resolution, and range for this study. The BOSE-DRS integrated system, shown in Figure 27, was used to indent tissue specimens following a displacement-controlled loading procedure while simultaneously measuring diffuse reflectance spectra. The DRS probe was held within a polycarbonate housing connected to the displacement cell of the ElectroForce®. Light was delivered from the light source to the specimens while the polycarbonate housing and probe tip moved with the actuated displacement cell downwards, compressing the tissue. Only the probe tip made contact with the skin. Specimens were placed beneath the probe tip on a glass slide that was rigidly fastened above a load cell via an aluminum adapter. A 12.5 mm diameter hole in the adapter beneath the glass sheet allowed light to be transmitted through the tissue to a large-area (1 cm x 1 cm) photodetector detecting 630 nm light from the tungsten halogen lamp (Newport Detector #818-ST and Optical Power Meter #1931-C, Irvine, CA). During compression, dynamic tissue thickness, load, light transmission, and diffuse reflectance spectra were recorded.

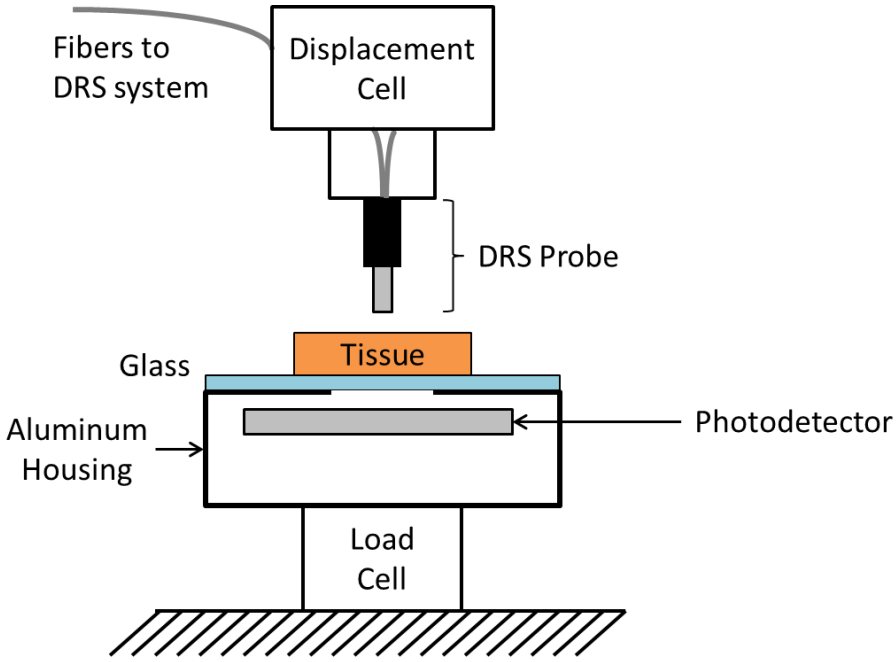

Figure 27. Integrated DRS-indentation system.

4.2.5 Mechanical Indentation Protocol and Data Analysis

A mechanical loading protocol was developed in order to study changes in diffuse reflectance spectra (and thus tissue optical properties) during tissue compression. The protocol consisted of linearly ramped, displacement-controlled compression at 1 mm/s to one of three final tissue thicknesses (3.0 mm, 2.0 mm, 1.0 mm) followed by a 120 second hold at constant displacement to evaluate additional thickness-independent effects of compression on tissue optical response. Before each trial, the position of the glass slide was determined by displacing the fiber probe tip downwards until it made contact with the glass slide, and this position, x_g, was recorded. Contact was defined as the position at which the load magnitude exceeded 0.01 N. After the probe tip was returned to its original position, a tissue specimen was placed on the glass slide and the indentation protocol was performed. The contact position of the top surface of the specimen, x_c, was calculated in post-processing following the same load threshold definition used in determining glass slide position. Dynamic tissue thickness, $T(t)$, was then calculated as

$$T(t) = \left(x_c - x_g\right) - x(t) \qquad \text{Eq. (18)}$$

where $x(t)$ is the measured displacement signal at time t. We also define a compressive tissue strain, e, the relative deformation of the compression tissue specimen region written as

$$e = \frac{|T(t) - T_0|}{T_0} \quad \text{Eq. (19)}$$

where T_0 is initial tissue thickness. Applied load, displacement, and light transmission were recorded at 10 Hz using WinTest®, proprietary control software for the Electroforce system. Diffuse reflectance spectra were acquired with an integration time of 100 ms, resulting in a 10 Hz sampling frequency. These spectra were recorded using SpectraSuite® Spectroscopy Platform, proprietary control software for the spectrometer.

4.2.6 DRS Data Analysis

Specimen optical properties were obtained by fitting diffuse reflectance spectra to a lookup table-based (LUT) inverse model, discussed in detail elsewhere [79, 82]. Diffuse reflectance was calculated as

$$R_{diffuse}(\lambda) = \frac{I_{sample}(\lambda) - I_{dark}(\lambda)}{I_{standard}(\lambda) - I_{dark}(\lambda)} \times 100\% \quad \text{Eq. (20)}$$

where $I_{sample}(\lambda)$ is the broadband light intensity measured from the tissue sample, $I_{dark}(\lambda)$ is a background spectrum measurement recorded with the light source turned off, and $I_{standard}(\lambda)$ is a measured spectrum from a NIST-traceable reflectance standard (Spectralon SRS-99-020, Labsphere, Inc.; North Sutton, NH). Subtracting the dark spectrum eliminates the effects of CCD dark current and ambient light, while wavelength-dependent system response is eliminated by normalizing sample response to a reflectance standard. In addition, daily differences in measurements due to variations in source intensity and system response were accounted for by regular calibration measurement of a standard solution of 1 μm diameter polystyrene microspheres (0.12%; Polysciences, Warrington, Pennsylvania) in water. Applying Equation (3) to this microsphere sample yields the microsphere solution reflectance, $R_{spheres}(\lambda)$. This calibration ensured that measured changes in diffuse reflectance were due only to changes in tissue optical properties. The calibrated diffuse reflectance spectra for each intensity measurement was then calculated as

$$R_{calibrated}(\lambda) = R_{diffuse}(\lambda) \times \frac{R_{spheres\ (LUT)}(\lambda)}{R_{spheres}(\lambda)} \quad \text{Eq. (21)}$$

where $R_{spheres\ (LUT)}(\lambda)$ was calculated with Equation (3) from a solution of polystyrene microspheres on the same day of the creation of the LUT. Following this procedure, all reflectance measurements were calibrated to the LUT model for extraction of optical properties.

To reduce computational costs, we chose to only perform the LUT fitting at 630 nm, rather than over a broader spectrum. From this fitting process we extracted the calculated reduced scattering coefficient.

4.3 Results

4.3.1 Light Transmission Results

Figure 28 shows data representing the trends seen in all compression trials. Given a linear displacement ramp followed by a held thickness, stress relaxation was observed, with the applied load necessary for maintaining fixed tissue thickness decreasing over time. We define a relative percent increase in light transmission as

$$Relative\ Transmission\ Increase = \frac{I_{peak} - I_{hold}}{I_{peak}} * 100\% \qquad \text{Eq. (22)}$$

where I_{peak} is the amount of light transmitted through the specimen when tissue thickness initially reached the specific thickness condition (at peak load) and I_{hold} is the amount of light transmitted after the hold at constant thickness. The average relative percent increase in light transmission for each final thickness group is shown in Figure 29. All transmission values increased at higher strains as tissue specimens were made thinner up to peak load. However, the additional dynamic increase in transmission continued during fixed tissue geometry conditions and greater relative increases were observed at higher strains.

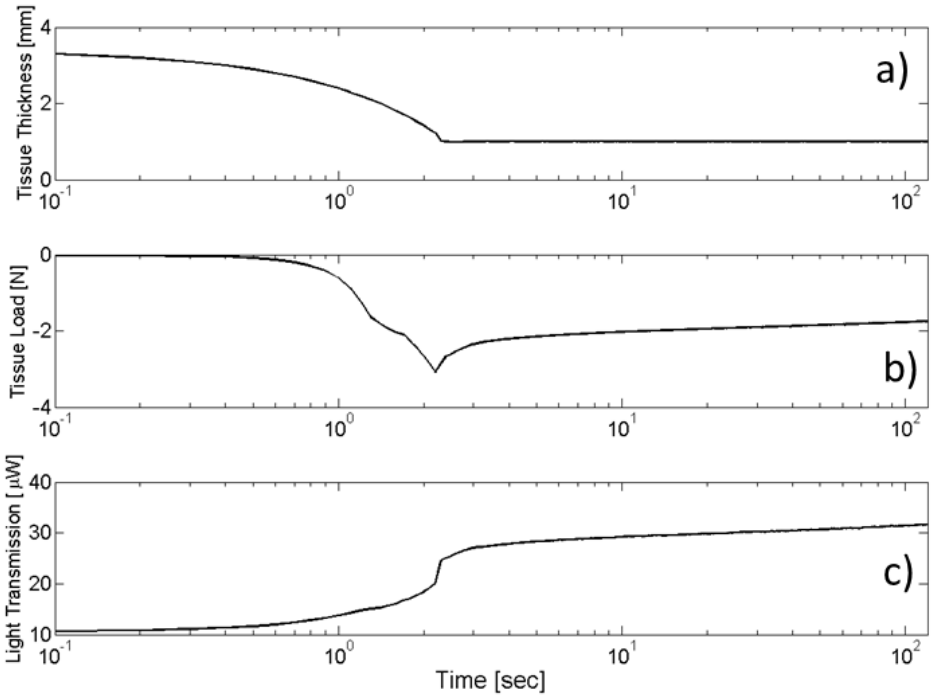

Figure 28. Representative results showing dynamic a) tissue thickness, b) tissue load, and c) light transmission through a representative tissue specimen over 120 seconds.

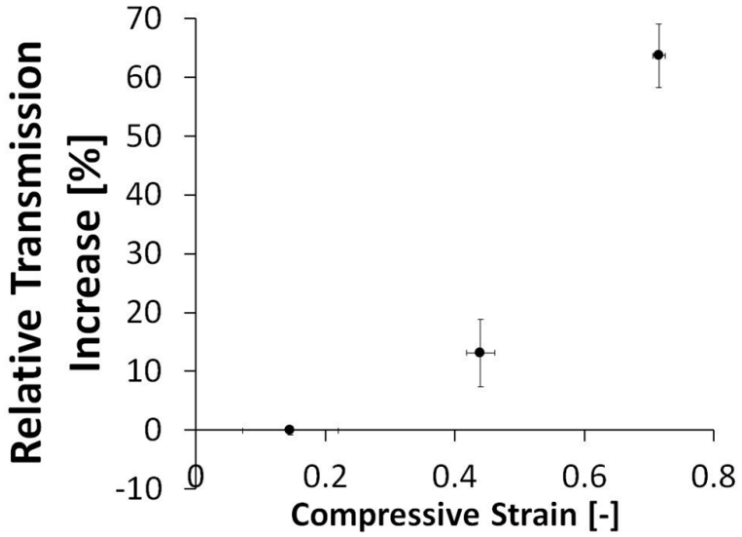

Figure 29. Relative transmission increases between peak load and end of hold. Error bars indicate 95% confidence interval.

4.3.2 Diffuse Reflectance Spectra Results

While diffuse reflectance spectra were recorded at 10 Hz (100 ms integration time) we chose to select three specific spectra per specimen for calculating tissue optical properties. These spectra were selected as 1) initial contact, 2) peak load (end of displacement ramp), and 3) the end of the 120 second hold. Figure 30 shows a representative image of reflectance spectra for one specimen from each final thickness group. All specimens experienced an increase in reflectance between initial contact and the peak load. Since specimens were preloaded close to the load threshold defining contact, tissue specimens may have relaxed or crept slightly under the pin before displacement began, causing loss of contact or initial optical clearing effects. Increase in reflectance between initial contact and the end of the displacement ramp may have also been due to focusing effects as the probe establishes contact with the tissue. Between the peak load and the end of the hold period, reflectance spectra decreased, with greater relative change corresponding to higher strain.

4.3.3 Dynamic Changes in Optical Properties

The reduced scattering coefficient was calculated from the LUT fitted spectra at 630 nm for each peak and end-of-hold spectrum. The relative decrease in scattering coefficient between peak load and end-of-hold was quantified as a percent change from the peak load value. Figure 31 shows greater reduction in scattering coefficient at higher strains, while lower strain does not significantly lower the scattering coefficient. The horizontal error bars corresponding to strain in Figure 31 begin large at low strain because variance in initial tissue thickness can alter the calculated strain. However, at higher strains this error decreases considerably. However, at very high strains the amount of optical clearing occurring is more variable, possibly due to variances in tissue properties that would have averaged out in less confined conditions, or perhaps due to damage caused by high-strain indentation. These results indicate that moderate compression to 0.45 compressive strain could still reduce scattering by as much as ~15%.

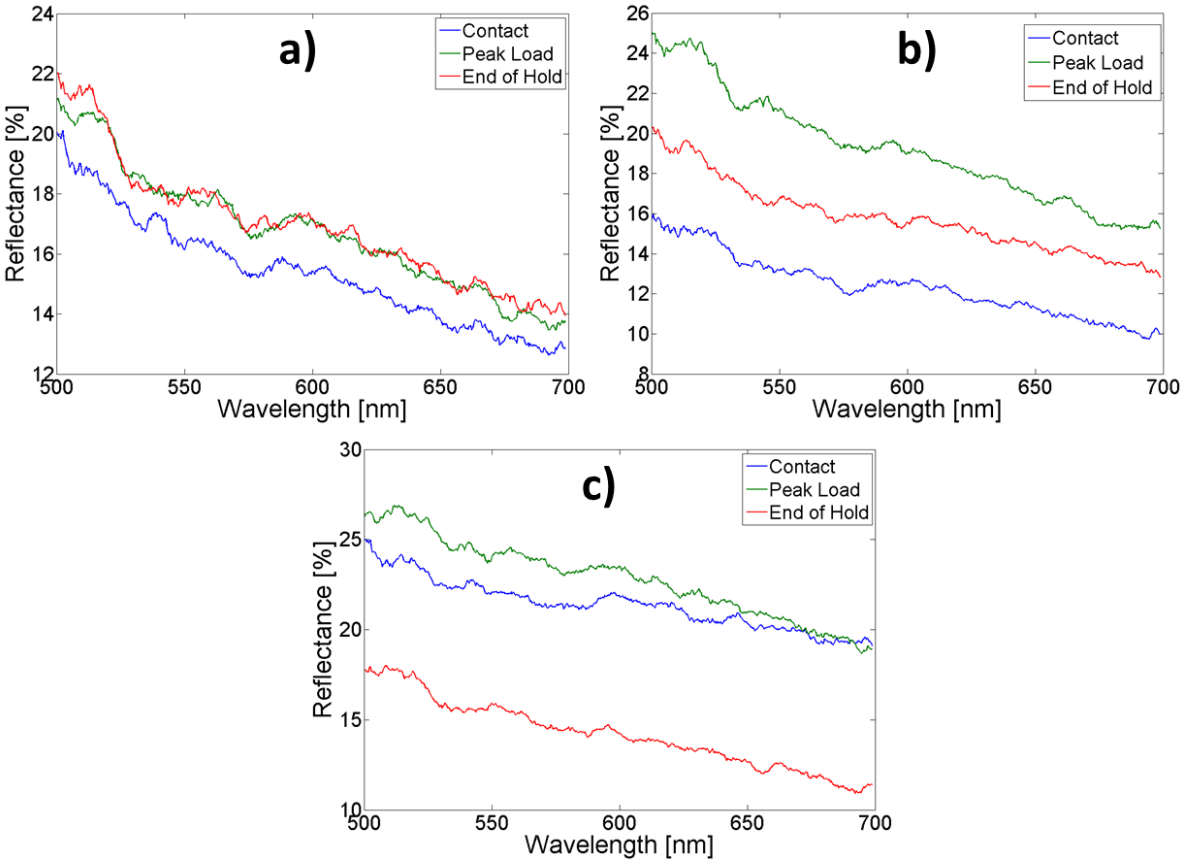

Figure 30. Representative reflectance spectra for indented final thicknesses of a) 3.0 mm, b) 2.0 mm, and c) 1.0 mm. The chronological order of spectra as recorded was contact, peak load, and end of hold.

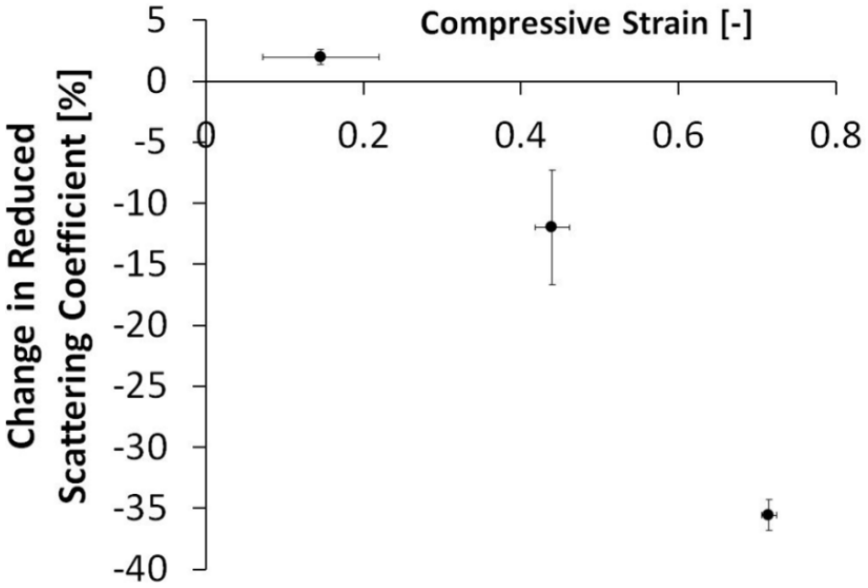

Figure 31. Relative decrease in reduced scattering coefficient between peak load and end of hold as a function of tissue strain. Error bars indicate 95% confidence intervals.

4.4 Discussion

These experimental results demonstrate that tissue strain is strongly correlated with decreased reduced scattering coefficient during indentation. Previous work by our group has demonstrated that mechanical optical clearing is a transient, strain-dependent effect [49] and our results in this study also show a positive correlation between tissue strain and light transmission increases. With load-controlled compression, changes in optical properties are not easily decoupled from dynamic changes in tissue thickness and geometry. Displacement-controlled compression enabled observation of thickness-independent optical property changes due to transient stress relaxation. These results show that as a tissue undergoes stress relaxation at fixed thickness, optical signals change, with transmission increasing and reflectance decreasing. While a change in reflectance during the displacement ramp was observed, likely due in part to thickness change and effects of interrogating different tissue layers, transient changes during the constant thickness portion of the procedure were also evident, supporting our hypothesis that changes in intrinsic tissue optical properties also occur. The decrease in reflectance with increasing wavelength is likely due to decreased scattering at longer wavelengths and the fact that the relatively short fiber separation distance of our probe is more sensitive to shorter wavelengths, resulting in lower intensities at longer wavelengths.

Our study employed the use of high-resolution load and displacement cells, allowing accurate monitoring of probe contact pressure and tissue thickness. Pressures in our study were significantly higher than those used in studies by other researchers, reaching a maximum of ~10 MPa, while most probe pressure effect studies to date have used pressures between ~0.01 MPa to ~0.20 MPa. [78, 83, 86]. For clinical applications, we must determine what range of loads and strains is acceptable in terms of tissue damage and pain experienced by the patient in a clinical setting. Studies investigating pain thresholds in various anatomical locations have reported pain thresholds between 0.5 and 1.1 MPa depending on anatomical location [89-91]. While some of our peak loads cause pressures up to 10 MPa, more moderate loading/strain conditions supply pressure of only ~2 MPa. These pressure estimates from our study are also based on peak dynamic load, while the residual load after relaxation is generally lower by ~40%.

4.5 Conclusion

These results show that indentation can be used as an optical clearing technique as described in previous work [45, 46, 48, 49]. This study shows for the first time the extent to which indentation can affect the intrinsic optical properties of tissue, particularly the reduction of light scattering, and the results suggest that the degree of this effect is significant. In addition to enhancing optical clearing effects, mechanical indentation may serve as a novel diagnostic platform in and of itself. Using combined DRS and mechanical indentation, we have demonstrated the potential for simultaneous monitoring of tissue mechanical and optical responses as well as intrinsic optical properties during mechanical deformation, in particular during stress relaxation. Results indicate that high-strain indentation significantly decreases tissue scattering, and thus support the hypothesis that optical clearing effects due to localized mechanical compression are a coupled phenomenon of tissue thinning and altered optical properties. Changes in optical properties may be attributed to transient local tissue dehydration through lateral water expulsion and removal or redistribution of light scattering and absorbing chromophores. Mechanical indentation modifies tissue optical properties and may be harnessed as a minimally-invasive optical clearing technique to improve optical diagnostics and therapeutics.

Chapter 5. Applications in Functional Near-Infrared Spectroscopy

5.1 Introduction

Diffuse Optical Tomography (DOT) is a low-cost, portable, and non-invasive optical sensing technology with broad applications, including cancer detection [82, 92, 93], muscle oximetry [94], atherosclerotic plaque analysis [95], evaluating stroke physiology [96, 97], brain-computer interfaces [98], neuro-rehabilitation [99], and cognitive neuroscience [100, 101]. For functional brain imaging, DOT using near-infrared light (commonly known as near-infrared spectroscopy or NIRS) measures dynamic changes in cerebral blood oxygenation, which is known to strongly correlate with neural activation and function. NIR light is delivered from a source (LED or fiberoptic) through the scalp and skull to the outer cortex, and the relative amount of light that is remitted to a nearby detector enables calculation of diffuse reflectance as a percentage of input light intensity. Functional MRI (fMRI), a prevalent technique in functional brain imaging, is mainly sensitive only to changes in deoxy-hemoglobin concentration [102]. In contrast, NIRS is capable of measuring relative changes in oxy-hemoglobin (HbO2), deoxy-hemoglobin (HHb), and total hemoglobin (tHb) concentrations by delivering light at multiple NIR wavelengths. NIRS offers many advantages over fMRI; NIRS systems are cheaper, costing $30,000-150,000 compared to $1-4 million for an MRI machine, may be used with subjects that are incompatible with an MRI environment (*e.g.* subjects with pacemakers or electronic neurostimulators), and offer higher temporal resolution (1-100 Hz [103] vs. 0.5-2.0 Hz [104]).

The major limitations of NIRS include lower spatial resolution (10-40 mm) fixed by sensor array geometry and shallow penetration depth (5-15 mm) caused by tissue absorption and scattering which limits sensing to the outermost layers of the cortex. Third and perhaps most importantly, because light must first pass through the outer tissue layers, scalp perfusion has been acknowledged as a significant confounding factor in NIRS, making relation of measured signals to cerebral hemodynamics challenging [105-109]. Attempts to reduce this error source include signal processing techniques [110, 111] and increasing the number of device sensors to allow for shallow, scalp-isolating sensing pairs in addition to brain-sensitive pairs [106, 112], but these methods substantially increase device hardware and software costs.

Tissue optical clearing is an emerging research area that enables reversible changes in optical absorption and scattering behavior in turbid tissues, improving light delivery for

diagnostic and therapeutic applications. Tissue optical clearing research has focused primarily on delivery of exogenous chemicals such as glycerol or dimethyl sulfoxide [6, 10, 12], but these invasive treatments pose safety concerns for *in vivo* studies, and the effects are limited by the low permeability of tissues. Mechanical tissue optical clearing, or MOC, is a reversible noninvasive technique we have pioneered for improving light-based diagnostic and therapeutic technologies. MOC is noninvasive, rapidly reversible (within 5-15 minutes), and has been shown to outperform chemical immersion techniques in an imaging study [49]. By mechanically loading (compressing) tissues, light delivery into deep tissue regions can be increased by ~2-3 fold [46]. This effect is attributed to changes in tissue optical properties due to interstitial water and blood movement [45]. Mechanical compression increases local interstitial pressure, displacing water and blood laterally within the tissue and modifying tissue optical properties such as refractive index [48] and absorption and scattering coefficients [113] in the indented region. MOC has been also shown to increase imaging resolution and contrast through turbid tissues [49]. These changes in optical properties alter measured extrinsic optical signals, including reflectance and transmittance. This effect has been observed *ex vivo* and *in vivo*, with the effect being reversible in live tissue. Others have observed this effect when applying manual pressure to optical probes, but the effects were dismissed as a 'source of error', and were not seen as useful dynamic tissue effects [78, 84, 86].

We have recently applied MOC to diffuse reflectance spectroscopy (DRS), a subdivision of DOT that does not focus on imaging, with results indicating that MOC effects are distinct from focusing effects or tissue thickness reduction [113] (see Chapter 4). A flat two-fiber optical probe was used to mechanically indent *ex vivo* porcine skin samples while measuring optical reflectance and transmittance. As samples were held at constant compressed thickness, reflectance continued to decrease which transmission increased, demonstrating that MOC must create intrinsic tissue changes. Because DRS, NIRS, and DOT are similar in principle, MOC is equally applicable to general reflectance-mode spectroscopies and imaging modalities, including optical coherence tomography, DRS, and confocal endoscopy.

The goal of this study is to develop an enhanced NIRS system using innovative technology described below to measure hemodynamic correlates of neural activity with 1) better mitigation of scalp perfusion, 2) deeper tissue penetration, and 3) higher spatial resolution than existing NIRS systems. Our specific demonstration of this will be an enhanced NIRS system that

can measure hemodynamic correlates of neural activity. The results of this study will generalize well beyond neural hemodynamic measurements to encompass the full range of non-invasive, portable applications of DOT.

Cognitive function creates spatially varying cerebral oxygenation changes related to specific regional and network changes in neural activity in the brain, but the effects of MOC-NIRS and standard NIRS will first be compared against a robust change in gray matter hemodynamics using breath-holding [114-116]. We will construct a MOC-NIRS prototype that uses translucent indenters to perform optical clearing of the scalp while allowing light delivery to the brain. This device is hypothesized to reach deeper regions of the brain as well as improve signal-to-noise ratio and sensitivity to cerebral hemodynamics. NIRS takes advantage of the relatively low absorption and scattering of tissue in the NIR range to deliver light through the many overlying tissue layers above the brain and into the brain itself (Figure 32). A certain percentage of the delivered light is remitted to a detector some distance away from the light source. Those photons that reach the detector have traveled through a 'banana-shaped' region in the tissue. The dominant tissue chromophores in the NIR range are HbO2 and HHb; By using two NIR wavelengths (typically ~700 nm and ~850 nm), HbO2 and HHb concentrations can be both calculated using a modified version of Beer's Law, in similar fashion to classical pulse oximetry [117].

To test the hypothesis that MOC-NIRS produces different signals compared with standard NIRS, measurements will be taken using both devices during a breath holding exercise. Breath holding elicits a non-neuronal blood oxygenation level dependent (BOLD) response throughout gray matter in the entire brain, removing any large spatial variance in signal. During breath holds, there are competing effects; tissue oxygen supplies are consumed, but an increase in global cerebral flow occurs through vasodilation in the brain in response to hypercapnia [115].

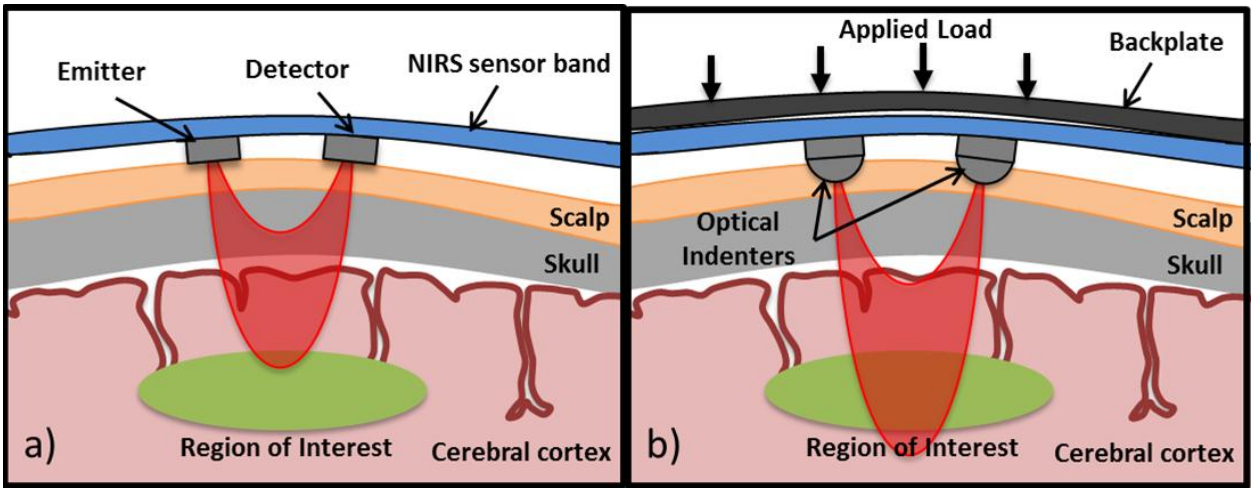

Figure 32. a) Standard NIRS configuration. b) MOC-NIRS configuration, with translucent glass indenters affixed to the optical components. These curved indenters cause mechanical optical clearing and create a focusing effect. Both these effects result in deeper light penetration.

5.2 Methods

5.2.1 MOC-NIRS Prototype Development

In this study we seek to integrate mechanical optical clearing technology with a commercially available fNIRS device (fNIR Devices, Ltd, Figure 38a). Several MOC-NIRS prototypes were developed and iterated upon in order to produce a NIRS device with integrated optical indenters to perform mechanical optical clearing of the scalp. In an earlier prototype, we epoxied an array of glass hemispherical indenters to a rigid polycarbonate substrate, which was wrapped against the forehead using straps (Figure 33). The fNIRS sensor band could then be placed over the indenter array, allowing NIR light to transmit through the glass indenters and polycarbonate plate. However, the rigidity of the polycarbonate prevented uniform loading and conformation to the head. To improve conformity, the indenters were instead adhered to a NIR-transparent plastic film wrapped around the NIRS sensor band (Figure 35b). A system of multiple smaller polycarbonate bands was placed over the NIRS sensor band and tightened in order to load the indenters from the back surface of the NIRS sensor band. The two straps can be independently tightening to distribute load over different portions of the indenter array (Figure 34). This prototype was used to collect preliminary experimental data (see Section 5.3). A more recent prototype has been developed that uses a rubber backplate instead of polycarbonate; this material selection allows for improved conformity, but the thickness of the rubber prevents mechanical force from being wasted in stretching the rubber rather than transferring load to the indenter array. This concept has also been recently extended to a device using two rubber plates

to more evenly distribute loading over the indenters (not shown). The two rubber plates were tightening using ropes instead of straps; by using rope, more of the load is delivered orthogonal to the rubber backplate and indenters, rather than the more horizontal loading that straps generate.

Figure 33. Early MOC-NIRS prototype with indenters epoxied to a rigid polycarbonate plate. a) Device applied to forehead, b) NIRS sensor band overlaid on top of indenter array. c) Indentation pattern after removal of device. Note non-uniform deformation, with some emitter/detector regions having undergone almost no optical clearing.

Figure 34. Prototypical MOC-NIRS device using two rigid polycarbonate loading bands overlaid on the NIRS sensor band. a) Device applied to forehead in a volunteer. b) Indentation pattern left after removal of device.

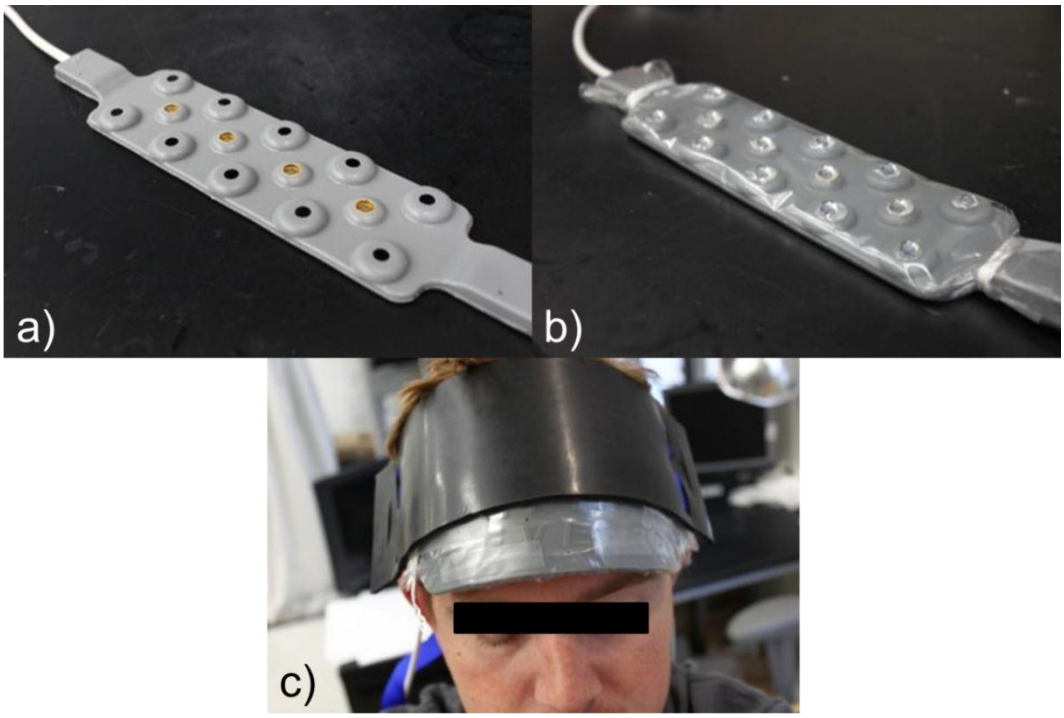

Figure 35. a) Commercial NIRS sensor with 4 emitters (center row) and 10 detectors (outer rows). b) NIRS sensor with integrated MOC-NIRS components, showing overlaid indenter array on a NIR-transparent plastic film. c) Device applied to forehead during data acquisition, with backplate raised to show MOC-NIRS sensor underneath.

5.2.2 Calculation of Hemoglobin Concentration Changes

After being placed on the human subject, the fNIRS device first takes a baseline measurement for each channel averaged over 10 seconds. The attenuation or optical density (*OD*) for each wavelength is then estimated from a modified form of the Beer-Lambert Law [117] as

$$OD = -\log\left(\frac{I}{I_0}\right) \qquad \text{Eq. (23)}$$

where I is the measured optical intensity and I_0 is the baseline optical intensity. The changes in chromophore concentration relative to baseline measurements, ΔHHb and ΔHbO_2 [µM], are then calculated as

$$\Delta HHb = c\frac{OD_{850}\varepsilon_{HbO_2,730} - OD_{730}\varepsilon_{HHb,850}}{\varepsilon_{HbO_2,730}\varepsilon_{Hb,850} - \varepsilon_{HbO_2,850}\varepsilon_{HbO_2,730}}$$
$$\Delta HbO_2 = c\frac{OD_{850}\varepsilon_{HbO_2,730} - OD_{730}\varepsilon_{HHb,850}}{\varepsilon_{HbO_2,730}\varepsilon_{Hb,850} - \varepsilon_{HbO_2,850}\varepsilon_{HbO_2,730}} \qquad \text{Eq. (24)}$$

where $\varepsilon_{X,\lambda}$ is the extinction coefficient for chromophore X at wavelength λ, OD_λ is the optical density and wavelength λ , and c is an empirical correction factor specific to the fNIRS device used. It should be noted that these calculations only produce relative changes in chromophore with respect to the baseline, not the absolute concentrations.

5.2.3 Breath-Holding Experiment

For breath holding experiments, each human subject was asked to perform two breath-holding exercises, in counter-balanced order: one using a standard commercial NIRS device and the other using the integrated MOC-NIRS device. Subjects were instructed to keep their eyes closed for the duration of the test and minimize any movement or speech. After recording baseline measurements over 10 seconds, each subject was instructed to perform 8 cycles of breath-holding, holding his/her breath for 15 seconds followed by 15 seconds of normal breathing.

Subjects may potentially experience discomfort/pain during the application of the MOC-NIRS headband with the optical clearing indenter array due to the applied compressive stress on the scalp, and such discomfort may affect neural activity. Subjects were asked to report any pain during application and/or measurements, which would result in immediate removal of the headband. Afterwards, subjects would be asked to rate any pain experienced on a visual analog scale [34]. The pain threshold for indentation is expected to be ~0.5-1.0 N/mm2 [35-37]. Since each indenter's contact surface area is typically ~9 mm2 under typical loading, indenter loads above ~3-4 N should be avoided.

5.3 Results and Discussion

We have acquired preliminary data using a simple MOC-NIRS prototype for subjects (N=4) following the breath-holding protocol. These data show that MOC-NIRS does modify the extrinsic signals and resulting Hgb calculations, with increased average signal intensity, increased signal-to-noise ratio, and improved agreement across multiple channels. Results showed that indentation increased raw signal intensity by 85 ± 35%, and that indentation increased amplitude of hemoglobin changes during breath cycles by 313% ± 105%. While the frequency content of the oxygenation signals has better agreement with the stimulus frequency of 0.033 Hz (as evaluated using the Fast Fourier Transform), the increase in signal intensity is more

difficult to explain. It could be that optical clearing and focusing effects reduce attenuation in the scalp, or that the detector indenters are collecting more shallow light, which is undesirable. Mathematical simulations will be able to explore these competing effects. These results suggest that indentation improves sensing of cerebral blood oxygenation, and may potentially enable sensing of deeper brain tissues, although mathematical analysis is needed to confirm that the apparent improvements in signal quality actually reflect increased sensitivity to cerebral tissue. In the future, calibrated springs could be installed in-line with the tightening straps or ropes so that the manually applied load can be repeated in different subjects.

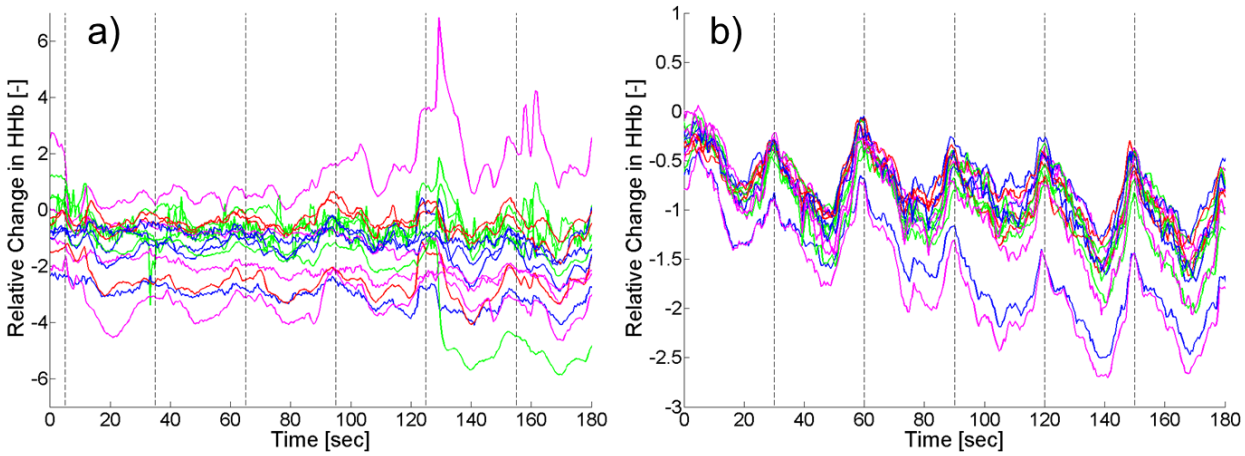

Figure 36. Preliminary fNIRS data collected during a breath-hold exercise a) with standard NIRS headgear and b) with integrated mechanical optical clearing indenter array. Data collected using rigid 2-strap design in Figure 34.

Figure 37. Indentation patterns after application and removal of MOC-NIRS prototype shown in Figure 34. Note that the patterns in a) and c) are non-uniform, while those in b) and d) exhibit better load distribution.

5.4 Conclusions

Results from this study indicate that mechanical optical clearing modifies measured fNIRS cerebral oxygenation signals compared with measurements using a standard available fNIRS system. These data suggest that optical clearing of the scalp higher sensitivity to cerebral hemodynamics, but more work is needed to determine the mechanisms that describe how optical clearing modifies light transport through the brain and overlying tissues. Future work will focus on performing forward Monte Carlo simulations to study the relative contributions of these competing effects and to ascertain the reliability of MOC-NIRS measurements as indicators of cerebral hemodynamic response.

Chapter 6. Conclusions

6.1 Summary and Conclusions

Substantial progress has been made on the development of mechanical optical clearing. By developing a multidomain model that can reproduce experimentally observed changes in light transmission and reflectance, we were able to establish that interstitial water transport is a valid candidate for the mechanism behind mechanical optical clearing, and this complex physical system merits further investigation. This modeling framework could be used to guide mechanical optical clearing device design for specific optical applications and specific target tissues. By integrating a diffuse reflectance spectroscopy system with a mechanical load frame, we were able to measure, for the first time, decreases in intrinsic optical scattering during mechanical loading of tissue. Preliminary results in developing mechanical optical clearing devices for fNIRS are promising, and further device refinement will enable more robust results.

The results of these studies have allowed us to reach the following conclusions:

1) Mechanical optical clearing causes intrinsic changes in tissue optical properties,
2) Tissue mechanical and optical dynamics during mechanical deformation are mechanistically coupled, and
3) Mechanical optical clearing has the potential to improve optical diagnostics and enable deep tissue sensing for many diffuse optical imaging techniques.

These conclusions support the stated hypothesis of this work: that interstitial transport of tissue chromophores (*e.g.* water and blood) causes intrinsic optical property changes, reduces tissue optical absorption and scattering, and improves light delivery in diagnostic applications.

One of the most important conclusions of this work is that mechanical optical clearing has the broad potential to improve light transport for, in general, any biomedical technique utilizing light delivery and/or collection from ex vivo or in vivo tissues. Mechanical optical clearing has been shown here to modify sensing of cerebral hemodynamic signals, but this could be extended to any diffuse optical spectroscopic or tomographic technique. While the focus of this work was to develop mechanical optical clearing for diagnostic techniques, mechanical

optical clearing could easily be applied to therapeutic technologies that rely on light delivery for photo-thermal and photo-chemical effects.

6.2 Future Directions

6.2.1 Refinements to Mathematical Models of Mechanical Optical Clearing

To date, our modeling efforts have focused on predicting optical clearing effects for ex vivo tissues. This allowed us to remove any clearing effects due to blood transport, leaving water movement as the only active clearing mechanism. For in vivo applications, it will be important to reintroduce the effects of blood transport on optical properties, particularly absorption coefficients due to the powerful absorption spectra of the various hemoglobin species present in blood. Indentation will pinch off capillary and larger blood vessel flows, removing any dynamic changes in blood content or oxygenation, but this will also create a temporary blood accumulation at the periphery of the indented region, as can be seen in 'blanching', where light contact on the skin removes blood from the more superficial layers and the skin visibly changes color from the natural pigmentation to a whiter hue.

Also, our work has assumed modeled tissues to be isotropic, with random fiber orientation with respect to all coordinate axes. However, skin is generally anisotropic, usually less stiff in the thickness (vertical) direction and stiffer in the transverse (radial) axes. The stiffness also varies within the transverse plane, as exhibited in Langer's lines. Future models should incorporate this anisotropy, perhaps through the use of a classical Fung model or the Holzapfel-Ogden model. This will require more mechanical tissue characterization experiments; in particular, biaxial testing may be needed to reliably fit any anisotropic hyperelastic material law. Another important assumption in the model was that skin tissue was comprised of only a single material. However, skin is actually a complex heterogeneous, layered tissue, with each layer possessing different properties. For example, it is well known that the epidermis and dermis have different optical properties [70, 71], and that they also exhibit different mechanical behavior [118].

We also made assumptions about the optical response of tissues to mechanical compression. While refractive index changes are expected due to changes in pore geometry and fiber orientation and concentration, our models do not currently account for this effect. This is primarily due to the limitations of the IAD algorithm, which can only provide absorption and

scattering information. In addition to refractive index, the scattering anisotropy factor has been shown to change during chemical optical clearing [119], and this effect should be expected for mechanical clearing as well. However, the use of reduced scattering coefficients fit to optical characterization data lowers the error due to assuming a fixed value for anisotropy factor.

Many of the discussed additions to the model are needed because skin has been the studied tissue. However, applying this model to other tissues would allow the model to become simpler. For example, the model could be applied to investigation of optical clearing in tissues with more isotropic extracellular matrix structures, or in tissue mimics for regenerative medicine applications. The mechanical properties of anisotropic tissues, such as blood vessels and other tubular tissue structures have been extensively studied; the Fung and Holzapfel-Ogden constituent models were originally developed for blood vessel wall mechanics [75].

6.2.2 Applications in Nonlinear In Vivo Microscopy and Imaging

Chapter 4 discussed the use of diffuse reflectance spectroscopy for studying mechanical optical clearing effects, but mechanical optical clearing could also improve sensing for arbitrary deep-tissue fiber-based spectroscopies and imaging modalities. For any system where a probe is placed in contact with the tissue of interest, optical clearing effects could prove useful in improving signal quality and depth of penetration. Such systems generally fall under *in vivo* microscopic techniques, where the goal is to perform an ‘optical biopsy’, evaluating the disease state of a tissue region without requiring tissue excision and collection for diagnosis by a histopathologist. Mechanical optical clearing could prove useful for enabling reliable optical biopsies of deep lesions, particularly in the skin. This technique would also be highly beneficial for optical biopsies in the various internal luminal tissues of the body accessible by endoscopy, such as the esophagus, trachea, oral cavity, and gastrointestinal tract. However, because these internal lumina may freely displace under applied indenter pressure, studies will need to determine the optimum force to minimize free displacement, maximize optical clearing effects, and ensure safe loading to avoid rupture of the lumen.

6.2.3 Applications to Optical Therapeutics

This work focused on the development of mechanical optical clearing technology for optical diagnostics, but the original application for this technology was optical therapeutics.

Rylander *et al.* originally described mechanical clearing for aiding in deep light delivery for photo-thermal therapies, specifically the subcutaneous and fatty tissues beneath the skin [45]. Mechanical clearing can improve delivery depth, and because there is no need for photon collection, the integration of mechanical indentation geometry and optical paths is less restricted. Mechanical clearing could be useful for improving therapies such as photodynamic therapy, laser-induced photothermal therapy, and cosmetic laser surgeries, enabling treatment of deeper tissue regions.

6.2.4 Mathematical Simulation of MOC-NIRS

Preliminary data have shown that MOC-NIRS produces different signals than standard NIRS. However, it is unclear what mechanisms create these differences, and instrumentation cannot be optimized until we understand these effects. Knowledge of the relative contributions of the mechanism(s) of MOC-NIRS will enable device optimization, particularly indenter geometry, spacing, and applied loads. Several effects that must be considered include focusing/lensing caused by the indenters, changes in intrinsic optical properties in scalp tissue due to MOC, and the altered acceptance angle created by hemispherical detector surfaces compared with optical fibers. Signal changes may also be partly attributable to better optode/tissue contact due to indenter curvature. We have developed a novel mathematical framework for understanding the mechanisms of MOC in the mechanical and optical domains, capable of simulating mechanical tissue deformation, interstitial water transport, and light transport [74, 120] (see Chapter 3). This mathematical framework will be used to study the competing effects described and more robustly evaluate tissue light transport during application of MOC-NIRS.

Combined mechanical finite element modeling and optical Monte Carlo simulation could be used to predict interstitial water distributions resulting from indentation by MOC-NIRS devices. This model considers the scalp tissue to be a poroviscoelastic material consisting of a solid phase (extracellular matrix) and a liquid phase (water) that has been fit to mechanical characterization data acquired previously. Water volume fraction results will be mapped to optical absorption and scattering coefficient values using spectrophotometric data acquired previously (see Chapter 3). Tissue deformation and optical property distributions will be incorporated into optical Monte Carlo simulations. The advantage of using this mechanical

model is that MOC effects may be turned on/off, which cannot be performed in an experimental situation. The mechanical modeling approach and predictions of scalp tissue indentation by hemispherical indenters can be taken directly from indentation simulations in Chapter 3 because the skull provides the rigid boundary condition beneath the compressible soft tissue (scalp as opposed to skin tissue).

To perform optical simulation over the complex geometry of the human head with the MOC-NIRS device in contact, TIM-OS could be employed [121]. TIM-OS performs Monte Carlo simulations on a 3D mesh of tetrahedral elements; because the tetrahedra may be assigned different optical properties, the mesh can accurately capture complex optical such as the human head. We will perform simulations of both standard NIRS and MOC-NIRS devices following the schematic shown in Figure 38. The outputs of each model are the wavelength-specific percent reflectance, mean photon path of collected photons, and fluence distribution within the tissue. Since NIRS uses two wavelengths (750 nm and 830 nm), two Monte Carlo simulations must be performed in order to calculate simulated hemoglobin outputs. By varying simulated device geometry and tissue properties, the relative strength of each potential mechanism for MOC-NIRS can be studied. By optimizing the shape of the NIRS sensing volume (banana-shaped region), we will be able to improve MOC-NIRS devices. Our previous work quantitatively describes how intrinsic optical properties of soft tissue change during mechanical compression [48, 113]. By combining this knowledge with literature values for optical properties of tissues we have not characterized previously [122, 123], we can predict the average travelled path of collected photons and simulate measured output reflectance signals.

Assuming the absorption of gray/white matter to be only a function of HbO2 and HHb concentrations, the absorption coefficient of the brain layer can be expressed using a rule of mixtures [79, 81]. Then, the hemoglobin concentrations can be varied, and the resulting reflectance signal predicted for different spatial distributions and amplitudes of brain absorption. Simulations can be performed for each time slice, allowing simulation of temporal changes in NIRS signals. This will provide more information on how MOC-NIRS affects measured outputs and will be used to guide device optimization.

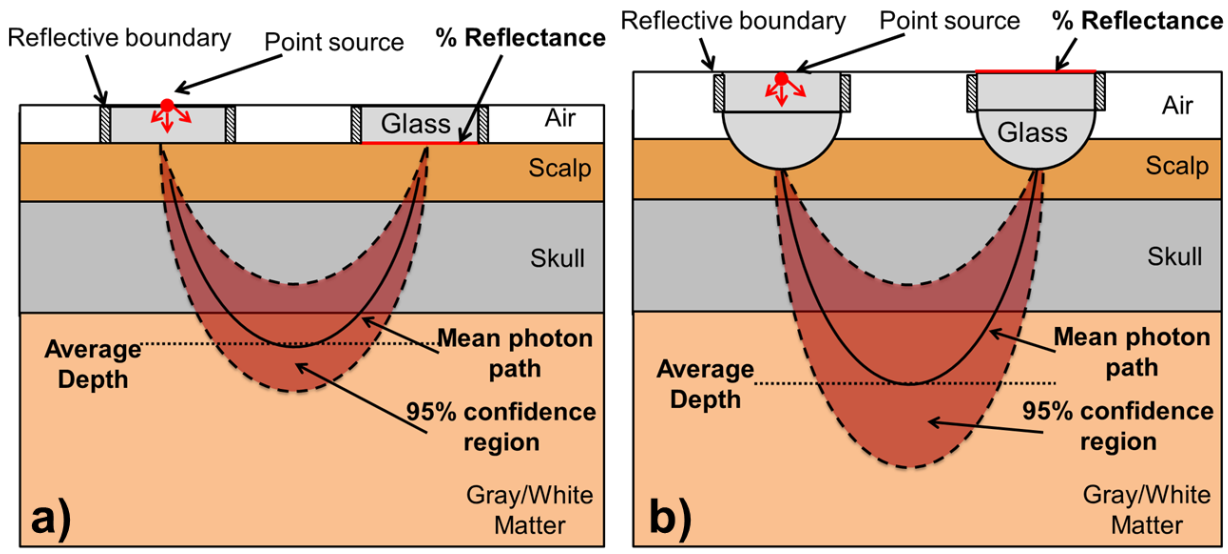

Figure 38. Schematic of Monte Carlo model, showing light source and detector, tissue regions, and MOC-NIRS sensor geometry for a) flat indenters and b) round indenters.

Simulations are expected to show a change in the shape of the sensing volume between the emitter and detector indenters, and we hypothesize that this sensitivity region will become taller with a greater average depth compared with standard NIRS. Output reflectance is expected to be greater for MOC-NIRS geometry compared with standard NIRS geometry based on preliminary data. If we can demonstrate that this model can calculate the NIRS sensing volume of an emitter/detector pair through a multi-layered tissue structure, we can attempt to model dynamic signal changes as a result of transient changes in cerebral oxygenation. For example, if Monte Carlo simulations were performed with the MOC-NIRS device at mechanical steady-state for multiple times, and if we alter the absorption coefficient due to a change in tissue oxygenation state, we could simulate a dynamic change in measured NIRS signal. In the future, we could also investigate the effects of partial regions changing within the sensing volume, as would occur in a functional study where neuronal activity created site-specific hemodynamic responses in the brain.

6.3. Pertinent Publications

6.3.1 Published Journal Articles

W. C. Vogt, A. Izquierdo-Román, B. Nichols, L. Lim, J.W. Tunnell, C.G. Rylander, "Effect of Mechanical Indentation on Diffuse Reflectance Spectra, Light Transmission, and Intrinsic Optical Properties in Ex Vivo Porcine Skin", *Lasers in Surgery and Medicine*, 44(4):303-9, 2012.

A. A. Gurjarpadhye, **W. C. Vogt**, Yajing Liu, and Christopher G. Rylander, "Effect of Localized Mechanical Indentation on Skin Water Content Evaluated Using OCT", *International Journal of Biomedical Imaging*, Volume 2011, 817250-1-8, 2011.

A. Izquierdo-Román, **W. C. Vogt**, Leeanna Hyacinth, and Christopher G. Rylander, "Mechanical Tissue Optical Clearing Technique Increases Imaging Resolution and Contrast Through Ex vivo Porcine Skin," *Lasers in Surgery and Medicine*, 43:814-823, 2011.

W. C. Vogt, H. Shen, G. Wang, C. G. Rylander, "Parametric Study of Tissue Optical Clearing by Localized Mechanical Compression using Combined Finite Element and Monte Carlo Simulation*," Journal of Innovative Optical Health Sciences*, 3(3): 1-9, 2010.

W. C. Vogt, C. G. Rylander, "Multidomain Modeling of Soft Tissue Indentation: Poroviscoelastic Tissue Behavior Influences Optical Transmission", to be submitted to the Journal of Biomechanical Engineering.

W. C. Vogt, C. G. Rylander, "Effects of Fiberoptic Probe Indentation Geometry on Light Transmission: Mechanical Optical Clearing is an Intrinsic Effect.", to be submitted to the Journal of Biomedical Optics

6.4 Pertinent Conference Proceedings

6.4.1 Podium Presentations

W. C. Vogt, C. G. Rylander, "Coupled Poroviscoelastic and Optical Monte Carlo Simulation of Dynamic Light Transport Through Indented Soft Tissue", ASME 2013 Summer Bioengineering Conference, Bend, OR, June 26, 2013.

W. C. Vogt, C. G. Rylander, "Effects of Mechanical Indentation Geometry on Skin Optical Properties and NIR Reflectance Measurements in the Human Brain". ASLMS Annual Conference 2013, Boston, MA, April 5, 2013.

Special Section Honoring Ken Diller: W. C. Vogt, C. G. Rylander, "Effects of Tissue Dehydration on Optical Diffuse Reflectance and Transmittance in Ex Vivo Porcine Skin", ASME 2012 Summer Bioengineering Conference, Fajardo, Puerto Rico, June 21, 2012.

W. C. Vogt, A. Izquierdo-Román, B. Nichols, L. Lim, J. W. Tunnell, C. G. Rylander, "Effects of Mechanical Indentation on Tissue Diffuse Reflectance Spectra and Light Transmission", ASLMS Annual Conference 2012, Kissimmee, FL, April 20, 2012.

W. C. Vogt, C. G. Rylander, "Multidomain Simulation of Mechanical Tissue Optical Clearing Devices: a Platform for Device Optimization". ASLMS Annual Conference 2011, Grapevine, TX.

W. C. Vogt, A. Izquierdo-Román, C. G. Rylander, "Tissue Optical Clearing Devices: Effects of Water Content on the Hyperelastic Mechanical Properties of Ex Vivo Porcine Skin". ASME Summer Bioengineering Conference, Naples, FL, June 17, 2010.

6.4.2 Poster Presentations

W. C. Vogt, E. Romero, S. M. LaConte, C. G. Rylander, "Mechanical Indentation Improves Cerebral Blood Oxygenation Signal Quality of Functional Near-Infrared Spectroscopy (fNIRS)

During Breath Holding", SPIE Photonics West (BiOS) 2013, San Francisco, CA, February 3, 2013.

W. C. Vogt, C. G. Rylander, "Dynamic Mechanical Optical Clearing Effects are Predicted by Coupled Mechanical and Optical Simulation of Tissue Poroviscoelastic Stress Relaxation", BMES Annual Meeting 2012, Atlanta, GA, October 25, 2012.

W. C. Vogt, C. G. Rylander, "Modeling Interstitial Water and Light Biotransport During Local Tissue Indentation with Optical Clearing Devices", BMES Annual Meeting 2011, Hartford, CT, October 14, 2011.

W. C. Vogt, A. Izquierdo-Román, C. G. Rylander, "Multidomain Modeling of Spatial Distributions of Tissue Optical Properties During Indentation: Mechanical Tissue Optical Clearing Devices as Diagnostic Tools," ASME 2011 Summer Bioengineering Conference, Farmington, PA, June 23, 2011.

W. C. Vogt, A. Izquierdo-Román, C. G. Rylander, "Combined Mechanical and Optical Simulation of Tissue During Application of Optical Clearing Devices," BMES 2010 Annual Meeting, Austin, TX, October 8, 2010.

References

1. Bradley WG, "History of medical imaging". *Proc Am Philos Soc*, 2008; **152**(3): 349-61.

2. Damadian R, "Tumor detection by nuclear magnetic resonance". *Science*, 1971; **171**(3976): 1151-3.

3. Brenner DJ, Doll R, Goodhead DT, Hall EJ, Land CE, Little JB, Lubin JH, Preston DL, Preston RJ, Puskin JS, Ron E, Sachs RK, Samet JM, Setlow RB, and Zaider M, "Cancer risks attributable to low doses of ionizing radiation: Assessing what we really know". *P Natl Acad Sci USA*, 2003; **100**(24): 13761-13766.

4. Wang LH and Wu H, *Biomedical Optics: Principles and Imaging*. 2007, Hoboken, New Jersey: John Wiley & Sons, Inc.

5. Cerussi A, Shah N, Hsiang D, Durkin A, Butler J, and Tromberg BJ, "In vivo absorption, scattering, and physiologic properties of 58 malignant breast tumors determined by broadband diffuse optical spectroscopy". *Journal of Biomedical Optics*, 2006; **11**(4).

6. Rylander CG, Stumpp OF, Milner TE, Kemp NJ, Mendenhall JM, Diller KR, and Welch AJ, "Dehydration mechanism of optical clearing in tissue". *Journal of Biomedical Optics*, 2006; **11**(4): 041117.

7. Fan CM and Yao G, "Imaging myocardial fiber orientation using polarization sensitive optical coherence tomography". *Biomedical Optics Express*, 2013; **4**(3): 460-465.

8. Anderson RR and Parrish JA, "The Optics of Human-Skin". *Journal of Investigative Dermatology*, 1981; **77**(1): 13-19.

9. Bashkatov AN, Genina EA, Kochubey VI, and Tuchin VV, "Optical properties of human skin, subcutaneous and mucous tissues in the wavelength range from 400 to 2000 nm". *Journal of Physics D-Applied Physics*, 2005; **38**(15): 2543-2555.

10. Tuchin VV, Maksimova IL, Zimnyakov DA, Kon IL, Mavlyutov AH, and Mishin AA, "Light propagation in tissues with controlled optical properties". *Journal of Biomedical Optics*, 1997; **2**(4): 401-417.

11. Tuchin VV, "Optical clearing of tissue and blood using immersion method". *Journal of physics. D, Applied physics*, 2005; **38**: 2497-2518.

12. Vargas G, Chan KF, Thomsen SL, and Welch AJ, "Use of osmotically active agents to alter optical properties of tissue: Effects on the detected fluorescence signal measured through skin". *Lasers in Surgery and Medicine*, 2001; **29**(3): 213-220.

13. Kang H, Son T, Yoon J, Kwon K, Nelson JS, and Jung B, "Evaluation of laser beam profile in soft tissue due to compression, glycerol, and micro-needling". *Lasers in Surgery and Medicine*, 2008; **40**(8): 570-575.

14. Galanzha EI, Tuchin VV, Solovieva AV, Stepanova TV, Luo Q, and Cheng H, "Skin backreflectance and microvascular system functioning at the action of osmotic agents". *Journal of Physics D-Applied Physics*, 2003; **36**(14): 1739-1746.

15. Xu XQ and Wang RKK, "The role of water desorption on optical clearing of biotissue: Studied with near infrared reflectance spectroscopy". *Medical Physics*, 2003; **30**(6): 1246-1253.

16. Vargas O, Chan EK, Barton JK, Rylander HG, and Welch AJ, "Use of an agent to reduce scattering in skin". *Lasers in Surgery and Medicine*, 1999; **24**(2): 133-141.

17. Genina EA, Bashkatov AN, Sinichkin YP, and Tuchin VV, "Optical clearing of the eye sclera in vivo caused by glucose". *Quantum Electron+*, 2006; **36**(12): 1119-1124.

18. Wang RKK, Xu XQ, He YH, and Elder JB, "Investigation of optical clearing of gastric tissue immersed with hyperosmotic agents". *Ieee Journal of Selected Topics in Quantum Electronics*, 2003; **9**(2): 234-242.

19. Xu XQ and Wang RKK, "Synergistic effect of hyperosmotic agents of dimethyl sulfoxide and glycerol on optical clearing of gastric tissue studied with near infrared spectroscopy". *Phys Med Biol*, 2004; **49**(3): 457-468.

20. Plotnikov S, Juneja V, Isaacson AB, Mohler WA, and Campagnola PJ, "Optical clearing for improved contrast in second harmonic generation Imaging of skeletal muscle". *Biophys J*, 2006; **90**(1): 328-339.

21. Bashkatov AN, Genina EA, Tuchin VV, and Altshuler GB, "Skin optical clearing for improvement of laser tattoo removal". *Laser Phys*, 2009; **19**(6): 1312-1322.

22. Khan MH, Choi B, Chess S, K MK, McCullough J, and Nelson JS, "Optical clearing of in vivo human skin: implications for light-based diagnostic imaging and therapeutics". *Lasers in Surgery and Medicine*, 2004; **34**(2): 83-85.

23. Wang RKK, "Signal degradation by coherence tomography multiple scattering in optical of dense tissue: a Monte Carlo study towards optical clearing of biotissues". *Phys Med Biol*, 2002; **47**(13): 2281-2299.

24. Wang RKK, Xu XQ, Tuchin VV, and Elder JB, "Concurrent enhancement of imaging depth and contrast for optical coherence tomography by hyperosmotic agents". *J Opt Soc Am B*, 2001; **18**(7): 948-953.

25. Larina IV, Carbajal EF, Tuchin VV, Dickinson ME, and Larin KV, "Enhanced OCT imaging of embryonic tissue with optical clearing". *Laser Phys Lett*, 2008; **5**(6): 476-479.

26. Proskurin SG and Meglinski IV, "Optical coherence tomography imaging depth enhancement by superficial skin optical clearing". *Laser Phys Lett*, 2007; **4**(11): 824-826.

27. Cicchi R, Pavone FS, Massi D, and Sampson DD, "Contrast and depth enhancement in two-photon microscopy of human skin ex vivo by use of optical clearing agents". *Opt Express*, 2005; **13**(7): 2337-2344.

28. Yeh AT and Hirshburg J, "Molecular interactions of exogenous chemical agents with collagen - implications for tissue optical clearing". *Journal of Biomedical Optics*, 2006; **11**(1).

29. Bolin FP, Preuss LE, Taylor RC, and Ference RJ, "Refractive-Index of Some Mammalian-Tissues Using a Fiber Optic Cladding Method". *Applied Optics*, 1989; **28**(12): 2297-2303.

30. Ding HF, Lu JQ, Wooden WA, Kragel PJ, and Hu XH, "Refractive indices of human skin tissues at eight wavelengths and estimated dispersion relations between 300 and 1600 nm". *Phys Med Biol*, 2006; **51**(6): 1479-1489.

31. Lees S, Tao NJ, and Lindsay SM, "Studies of Compact Hard Tissues and Collagen by Means of Brillouin Light-Scattering". *Connect Tissue Res*, 1990; **24**(3-4): 187-205.

32. Heller W, "Remarks on Refractive Index Mixture Rules". *Journal of Physical Chemistry*, 1965; **69**(4): 1123-1129.

33. Yeh AT, Choi B, Nelson JS, and Tromberg BJ, "Reversible dissociation of collagen in tissues". *Journal of Investigative Dermatology*, 2003; **121**(6): 1332-1335.

34. Hirshburg J, Choi B, Nelson JS, and Yeh AT, "Correlation between collagen solubility and skin optical clearing using sugars". *Lasers in surgery and medicine*, 2007; **39**(2): 140-144.

35. Hirshburg JM, Ravikumar KM, Hwang W, and Yeh AT, "Molecular basis for optical clearing of collagenous tissues". *Journal of Biomedical Optics*, 2010; **15**(5).

36. Stumpp O, Chen B, and Welch AJ, "Using sandpaper for noninvasive transepidermal optical skin clearing agent delivery". *Journal of Biomedical Optics*, 2006; **11**(4).

37. Genina EA, Dolotov LE, Bashkatov AN, Terentyuk GS, Maslyakova GN, Zubkina EA, Tuchin VV, Yaroslavsky IV, and Altshuler GB, "Fractional laser microablation of skin aimed at enhancing its permeability for nanoparticles". *Quantum Electron+*, 2011; **41**(5): 396-401.

38. Liu CH, Zhi ZW, Tuchin VV, Luo QM, and Zhu D, "Enhancement of Skin Optical Clearing Efficacy Using Photo-Irradiation". *Lasers in surgery and medicine*, 2010; **42**(2): 132-140.

39. Tuchin VV, Altshuler GB, Gavrilova AA, Pravdin AB, Tabatadze D, Childs J, and Yaroslavsky IV, "Optical clearing of skin using flashlamp-induced enhancement of epidermal permeability". *Lasers in surgery and medicine*, 2006; **38**(9): 824-836.

40. Jiang JY and Wang RKK, "Comparing the synergistic effects of oleic acid and dimethyl sulfoxide as vehicles for optical clearing of skin tissue in vitro". *Phys Med Biol*, 2004; **49**(23): 5283-5294.

41. Moulton K, Lovell F, Williams E, Ryan P, Lay DC, Jansen D, and Willard S, "Use of glycerol as an optical clearing agent for enhancing photonic transference and detection of Salmonella typhimurium through porcine skin". *Journal of Biomedical Optics*, 2006; **11**(5).

42. Xu XQ and Zhu QH, "Evaluation of skin optical clearing enhancement with Azone as a penetration enhancer". *Opt Commun*, 2007; **279**(1): 223-228.

43. Yoon J, Son T, Choi EH, Choi B, Nelson JS, and Jung B, "Enhancement of optical skin clearing efficacy using a microneedle roller". *Journal of Biomedical Optics*, 2008; **13**(2).

44. Xu XQ, Zhu QH, and Sun CJ, "Assessment of the effects of ultrasound-mediated alcohols on skin optical clearing". *Journal of Biomedical Optics*, 2009; **14**(3).

45. Rylander CG, Milner TE, Baranov SA, and Nelson JS, "Mechanical tissue optical clearing devices: Enhancement of light penetration in ex vivo porcine skin and adipose tissue". *Lasers in surgery and medicine*, 2008; **40**(10): 688-694.

46. Drew C, Milner TE, and Rylander CG, "Mechanical tissue optical clearing devices: evaluation of enhanced light penetration in skin using optical coherence tomography". *Journal of Biomedical Optics*, 2009; **14**(6): 064019.

47. Sorin WV and Gray DF, "Simultaneous Thickness and Group Index Measurement Using Optical Low-Coherence Reflectometry". *Ieee Photonic Tech L*, 1992; **4**(1): 105-107.

48. Gurjarpadhye A, Vogt WC, Liu Y, and Rylander CG, "Effect of Localized Mechanical Indentation on Skin Water Content Evaluated Using OCT". *International Journal of Biomed Imaging*, 2011.

49. Izquierdo-Roman A, Vogt WC, Hyacinth L, and Rylander CG, "Mechanical tissue optical clearing technique increases imaging resolution and contrast through Ex vivo porcine skin (vol 43, pg 814, 2011)". *Lasers in surgery and medicine*, 2011; **43**(10): 998-1007.

50. Askar'yan GA, "Enhancement of transmission of laser and other radiation by soft turbid physical and biological media". *SOV J QUANTUM ELECTRON*, 1982; **12**(7): 877-880.

51. Agrba PD, Kirillin MY, Abelevich AI, Zagaynova EV, and Kamensky VA, "Compression as a method for increasing the informativity of optical coherence tomography of biotissues". *Opt Spectrosc+*, 2009; **107**(6): 853-858.

52. Kirillin MY, Agrba PD, and Kamensky VA, "In vivo study of the effect of mechanical compression on formation of OCT images of human skin". *J Biophotonics*, 2010; **3**(12): 752-758.

53. Chan EK, Sorg B, Protsenko D, ONeil M, Motamedi M, and Welch AJ, "Effects of compression on soft tissue optical properties". *IEEE Journal of Selected Topics in Quantum Electronics*, 1996; **2**(4): 943-950.

54. Shangguan HP, S. A. , Jacques SL, Casperson LW, and Gregory KW, "Pressure Effects on Soft Tissues Monitored by Changes in Tissue Optical Properties". *Laser-Tissue Interaction IX, vol. 3254 of Proceedings of SPIE*, 1998: 366-371.

55. Rylander CG, Stumpp OF, Milner TE, Kemp NJ, Mendenhall JM, Diller KR, and Welch AJ, "Dehydration mechanism of optical clearing in tissue". *Journal of Biomedical Optics*, 2006; **11**(4).

56. Choi B, Tsu L, Chen E, Ishak TS, Iskandar SM, Chess S, and Nelson JS, "Determination of chemical agent optical clearing potential using in vitro human skin". *Lasers in Surgery and Medicine*, 2005; **36**(2): 72-75.

57. Izquierdo-Roman A, Vogt WC, and Rylander CG, "Mechanical tissue optical clearing technique increases imaging resolution and contrast through ex vivo porcine skin". *Lasers in Surgery and Medicine*, 2011; **43**(8): 814–823.

58. Abaqus Theory Manual 1992, Hibbitt, Karlsson, and Sorensen.

59. Prahl SA, Vangemert MJC, and Welch AJ, "Determining the Optical-Properties of Turbid Media by Using the Adding-Doubling Method". *Appl Optics*, 1993; **32**(4): 559-568.

60. Zienkiewicz OC and Taylor RL, *The finite element method*. 5th ed. 2000, Oxford ; Boston: Butterworth-Heinemann.

61. Mak AFT, Huang LD, and Wang QQ, "A Biphasic Poroelastic Analysis of the Flow Dependent Subcutaneous Tissue Pressure and Compaction Due to Epidermal Loadings - Issues in Pressure Sore". *J Biomech Eng-T Asme*, 1994; **116**(4): 421-429.

62. Li LP, Buschmann MD, and Shirazi-Adl A, "A fibril reinforced nonhomogeneous poroelastic model for articular cartilage: inhomogeneous response in unconfined compression". *J Biomech*, 2000; **33**(12): 1533-1541.

63. Simon BR, Liable JP, Pflaster D, Yuan Y, and Krag MH, "A poroelastic finite element formulation including transport and swelling in soft tissue structures". *J Biomech Eng-T Asme*, 1996; **118**(1): 1-9.

64. Suh JK and DiSilvestro MR, "Biphasic poroviscoelastic behavior of hydrated biological soft tissue". *J Appl Mech-T Asme*, 1999; **66**(2): 528-535.

65. Suh JKF, DiSilvestro MR, Zhu QL, Wong M, and Jurvelin JS, "Biphasic poroviscoelastic simulation of the unconfined compression of articular cartilage: I - Simultaneous

prediction of reaction force and lateral displacement". *J Biomech Eng-T Asme*, 2001; **123**(2): 191-197.

66. Hubbert MK and Darcy H, *The theory of ground-water motion and related papers*. 1969, New York,: Hafner. (various pages).

67. Jain RK, "Transport of molecules in the tumor interstitium: a review". *Cancer Res*, 1987; **47**(12): 3039-51.

68. Lai WM, Mow VC, and Roth V, "Effects of Non-Linear Strain-Dependent Permeability and Rate of Compression on the Stress Behavior of Articular-Cartilage". *J Biomech Eng-T Asme*, 1981; **103**(2): 61-66.

69. Wang LH, Jacques SL, and Zheng LQ, "Mcml - Monte-Carlo Modeling of Light Transport in Multilayered Tissues". *Comput Meth Prog Bio*, 1995; **47**(2): 131-146.

70. Dhawan AP, D'Alessandro B, and Fu X, "Optical imaging modalities for biomedical applications". *IEEE Rev Biomed Eng*, 2010; **3**: 69-92.

71. Welch AJ and van Gemert MJC, eds. *Optical-Thermal Response of Laser-Irradiated Tissue*. Lasers, Photonics, and Electro-optics, ed. Kogelnik H. 1995, Plenum Press: New York, New York.

72. Shen H and Wang G, "A tetrahedron-based inhomogeneous Monte Carlo optical simulator". *Phys. Med. Biol.*, 2010; **55**(4): 947-962.

73. Nakagawa N, Matsumoto M, and Sakai S, "In vivo measurement of the water content in the dermis by confocal Raman spectroscopy". *Skin Research and Technology*, 2010; **16**(2): 137-141.

74. Vogt WC, Shen H, Wang G, and Rylander CG, "Parametric Study of Tissue Optical Clearing by Localized Mechanical Compression using Combined Finite Element and Monte Carlo Simulation". *J Innov Opt Heal Sci*, 2010; **3**(3): 203-211.

75. Holzapfel GA, Gasser TC, and Ogden RW, "A new constitutive framework for arterial wall mechanics and a comparative study of material models". *J Elasticity*, 2000; **61**(1-3): 1-48.

76. Sung KB, Liang C, Descour M, Collier T, Follen M, Malpica A, and Richards-Kortum R, "Near real time in vivo fibre optic confocal microscopy: sub-cellular structure resolved". *J Microsc-Oxford*, 2002; **207**: 137-145.

77. Izquierdo-Roman A, Vogt WC, Hyacinth L, and Rylander CG, "Mechanical Tissue Optical Clearing Technique Increases Imaging Resolution and Contrast Through Ex vivo Porcine Skin". *Lasers in surgery and medicine*, 2011; **43**(8): 814-823.

78. Lim LA, Nichols B, Rajaram N, and Tunnell JW, "Probe pressure effects on human skin diffuse reflectance and fluorescence spectroscopy measurements". *Journal of Biomedical Optics*, 2011; **16**(1): 011012.

79. Rajaram N, Nguyen TH, and Tunnell JW, "Lookup table-based inverse model for determining optical properties of turbid media". *Journal of Biomedical Optics*, 2008; **13**(5): 050501.

80. Farrell TJ, Patterson MS, and Wilson B, "A diffusion-theory model of spatially resolved, steady-state diffuse reflectance for the noninvasive determination of tissue optical properties in vivo". *Medical Physics*, 1992; **19**(4): 879-888.

81. Zonios G, Perelman LT, Backman VM, Manoharan R, Fitzmaurice M, Van Dam J, and Feld MS, "Diffuse reflectance spectroscopy of human adenomatous colon polyps in vivo". *Applied Optics*, 1999; **38**(31): 6628-6637.

82. Rajaram N, Aramil TJ, Lee K, Reichenberg JS, Nguyen TH, and Tunnell JW, "Design and validation of a clinical instrument for spectral diagnosis of cutaneous malignancy". *Applied Optics*, 2010; **49**(2): 142-152.

83. Nath A, Rivoire K, Chang S, Cox D, Atkinson EN, Follen M, and Richards-Kortum R, "Effect of probe pressure on cervical fluorescence spectroscopy measurements". *Journal of Biomedical Optics*, 2004; **9**(3): 523-533.

84. Murphy BW, Webster RJ, Turlach BA, Quirk CJ, Clay CD, Heenan PJ, and Sampson DD, "Toward the discrimination of early melanoma from common and dysplastic nevus using fiber optic diffuse reflectance spectroscopy". *Journal of Biomedical Optics*, 2005; **10**(6): 064020.

85. Chen WL, Liu R, Xu KX, and Wang RKK, "Influence of contact state on NIR diffuse reflectance spectroscopy in vivo". *J Phys D Appl Phys*, 2005; **38**(15): 2691-2695.

86. Ti Y and Lin W-C, "Effects of probe contact pressure on in vivo optical spectroscopy". *Opt Express*, 2008; **16**(6): 4250-4262.

87. Douplik A, Shalaby D, and Wilson BC, "The spectral dependence of fiberoptic probe pressure on tissue during in vivo diffuse reflectance spectroscopy". *Biomedical Topical Meeting, OSA Technical Digest*, 2004: paper FG4.

88. Zonios G and Dimou A, "Modeling diffuse reflectance from semi-infinite turbid media: application to the study of skin optical properties". *Opt Express*, 2006; **14**(19): 8661-8674.

89. Lee WC, Zhang M, and Mak AF, "Regional differences in pain threshold and tolerance of the transtibial residual limb: Including the effects of age and interface material". *Arch Phys Med Rehab*, 2005; **86**(4): 641-649.

90. Fischer AA, "Pressure Tolerance over Muscles and Bones in Normal Subjects". *Arch Phys Med Rehab*, 1986; **67**(6): 406-409.

91. Xiong SP, Goonetilleke RS, Witana CP, and Rodrigo WDAS, "An indentation apparatus for evaluating discomfort and pain thresholds in conjunction with mechanical properties of foot tissue in vivo". *J Rehabil Res Dev*, 2010; **47**(7): 629-641.

92. McBride TO, Pogue BW, Gerety ED, Poplack SB, Osterberg UL, and Paulsen KD, "Spectroscopic diffuse optical tomography for the quantitative assessment of hemoglobin concentration and oxygen saturation in breast tissue". *Applied Optics*, 1999; **38**(25): 5480-5490.

93. Drezek RA, Richards-Kortum R, Brewer MA, Feld MS, Pitris C, Ferenczy A, Faupel ML, and Follen M, "Optical imaging of the cervix". *Cancer*, 2003; **98**(9): 2015-2027.

94. Yu GQ, Durduran T, Lech G, Zhou C, Chance B, Mohler ER, and Yodh AG, "Time-dependent blood flow and oxygenation in human skeletal muscles measured with noninvasive near-infrared diffuse optical spectroscopies". *Journal of Biomedical Optics*, 2005; **10**(2).

95. Moreno PR, Lodder RA, Purushothaman KR, Charash WE, O'Connor WN, and Muller JE, "Detection of lipid pool, thin fibrous cap, and inflammatory cells in human aortic atherosclerotic plaques by near-infrared spectroscopy". *Circulation*, 2002; **105**(8): 923-927.

96. Culver JP, Durduran T, Furuya T, Cheung C, Greenberg JH, and Yodh AG, "Diffuse optical tomography of cerebral blood flow, oxygenation, and metabolism in rat during focal ischemia". *J Cerebr Blood F Met*, 2003; **23**(8): 911-924.

97. Sakatani K, Murata Y, Fujiwara N, Hoshino T, Nakamura S, Kano T, and Katayama Y, "Comparison of blood-oxygen-level-dependent functional magnetic resonance imaging and near-infrared spectroscopy recording during functional brain activation in patients with stroke and brain tumors". *Journal of Biomedical Optics*, 2007; **12**(6).

98. Coyle SM, Ward TE, and Markham CM, "Brain-computer interface using a simplified functional near-infrared spectroscopy system". *J Neural Eng*, 2007; **4**(3): 219-226.

99. Arenth PM, Ricker JH, and Schultheis MT, "Applications of Functional Near-Infrared Spectroscopy (fNIRS) to neurorehabilitation of cognitive disabilities". *Clin Neuropsychol*, 2007; **21**(1): 38-57.

100. Ferrari M and Quaresima V, "A brief review on the history of human functional near-infrared spectroscopy (fNIRS) development and fields of application". *Neuroimage*, 2012; **63**(2): 921-935.

101. Strangman G, Boas DA, and Sutton JP, "Non-invasive neuroimaging using near-infrared light". *Biol Psychiat*, 2002; **52**(7): 679-693.

102. Ogawa S, Lee TM, Kay AR, and Tank DW, "Brain Magnetic-Resonance-Imaging with Contrast Dependent on Blood Oxygenation". *P Natl Acad Sci USA*, 1990; **87**(24): 9868-9872.

103. Ferrari M, Mottola L, and Quaresima V, "Principles, techniques, and limitations of near infrared spectroscopy". *Can J Appl Physiol*, 2004; **29**(4): 463-87.

104. LaConte SM, "Decoding fMRI brain states in real-time". *Neuroimage*, 2011; **56**(2): 440-54.

105. Murkin JM and Arango M, "Near-infrared spectroscopy as an index of brain and tissue oxygenation". *Br J Anaesth*, 2009; **103 Suppl 1**: i3-13.

106. Saager R and Berger A, "Measurement of layer-like hemodynamic trends in scalp and cortex: implications for physiological baseline suppression in functional near-infrared spectroscopy". *J Biomed Opt*, 2008; **13**(3): 034017.

107. Owen-Reece H, Elwell CE, Wyatt JS, and Delpy DT, "The effect of scalp ischaemia on measurement of cerebral blood volume by near-infrared spectroscopy". *Physiol Meas*, 1996; **17**(4): 279-86.

108. Davis SL, Fadel PJ, Cui J, Thomas GD, and Crandall CG, "Skin blood flow influences near-infrared spectroscopy-derived measurements of tissue oxygenation during heat stress". *J Appl Physiol*, 2006; **100**(1): 221-4.

109. Hillman EMC, "Optical brain imaging in vivo: techniques and applications from animal to man". *Journal of Biomedical Optics*, 2007; **12**(5).

110. Schelkanova I and Toronov V, "Independent component analysis of broadband near-infrared spectroscopy data acquired on adult human head". *Biomed Opt Express*, 2012; **3**(1): 64-74.

111. Kohno S, Miyai I, Seiyama A, Oda I, Ishikawa A, Tsuneishi S, Amita T, and Shimizu K, "Removal of the skin blood flow artifact in functional near-infrared spectroscopic

imaging data through independent component analysis". *J Biomed Opt*, 2007; **12**(6): 062111.

112. White BR and Culver JP, "Phase-encoded retinotopy as an evaluation of diffuse optical neuroimaging". *Neuroimage*, 2010; **49**(1): 568-577.

113. Vogt WC, Izquierdo-Roman A, Nichols B, Lim L, Tunnell JW, and Rylander CG, "Effects of mechanical indentation on diffuse reflectance spectra, light transmission, and intrinsic optical properties in ex vivo porcine skin". *Lasers Surg Med*, 2012; **44**(4): 303-9.

114. Li TQ, Kastrup A, Takahashi AM, and Moseley ME, "Functional MRI of human brain during breath holding by BOLD and FAIR techniques". *Neuroimage*, 1999; **9**(2): 243-9.

115. Stillman AE, Hu X, and Jeroschherold M, "Functional Mri of Brain during Breath-Holding at 4-T". *Magn Reson Imaging*, 1995; **13**(6): 893-897.

116. Thomason ME, Foland LC, and Glover GH, "Calibration of BOLD fMRI using breath holding reduces group variance during a cognitive task". *Hum Brain Mapp*, 2007; **28**(1): 59-68.

117. Delpy DT and Cope M, "Quantification in tissue near-infrared spectroscopy". *Philos T R Soc B*, 1997; **352**(1354): 649-659.

118. Hendriks FM, Brokken D, Oomens CWJ, Bader DL, and Baaijens FPT, "The relative contributions of different skin layers to the mechanical behavior of human skin in vivo using suction experiments". *Med Eng Phys*, 2006; **28**(3): 259-266.

119. Samatham R, Phillips KG, and Jacques SL, "Assessment of Optical Clearing Agents Using Reflectance-Mode Confocal Scanning Laser Microscopy". *J Innov Opt Heal Sci*, 2010; **3**(3): 183-188.

120. Vogt WC, Izquierdo-Roman A, and Rylander C, "Multidomain Simulation of Mechanical Tissue Optical Clearing Devices: A Platform for Device Optimization". *Lasers in Surgery and Medicine*, 2011; **43**: 915-915.

121. Shen H and Wang G, "A tetrahedron-based inhomogeneous Monte Carlo optical simulator". *Phys Med Biol*, 2010; **55**(4): 947-962.

122. Genina EA, Bashkatov AN, and Tuchin VV, "Optical Clearing of Cranial Bone". *Advances in Optical Technologies*, 2008; **2008**(ID: 267867).

123. Boas D, Culver J, Stott J, and Dunn A, "Three dimensional Monte Carlo code for photon migration through complex heterogeneous media including the adult human head". *Opt Express*, 2002; **10**(3): 159-70.